Heptacoordinate Tb^{3+} Complexes with 90% Quantum Yields: High-Performance Examples of Combined Singlet- and Triplet-to-Tb^{3+} Energy-Transfer Pathways

Lucas Emanoel do N. Aquino,[†] Guilherme A. Barbosa,[†] Jaqueline de L. Ramos,[†] Siddhartha O. K. Giese,[†] Francielli S. Santana, [†] David L. Hughes,[‡] Giovana G. Nunes,[†] Lianshe Fu,[§] Ming Fang,[§] Giordano Poneti,[⊥] Albano N. Carneiro Neto,[§] Renaldo T. Moura Jr.,[∥] Rute A. S. Ferreira,[§] Luís D. Carlos,*[,§] Andreia G. Macedo,*[,§,#] and Jaísa F. Soares*[,†]

[†]Department of Chemistry, Federal University of Paraná, 81530-900 – Curitiba-PR, Brazil

[‡]School of Chemistry, University of East Anglia, Norwich NR4 7TJ, UK

[§]Phantom-g, CICECO – Aveiro Institute of Materials, Department of Physics, University of Aveiro, 3810-193 – Aveiro, Portugal

[⊥]Institute of Chemistry, Federal University of Rio de Janeiro, 21941-909 – Rio de Janeiro-RJ, Brazil

[∥]Department of Chemistry and Physics, Federal University of Paraíba, 58397-000 – Areia-PB, Brazil

[#]Department of Physics, Federal University of Technology, 80230-901 – Curitiba-PR, Brazil

Corresponding author's email addresses:

lcarlos@ua.pt (Luís D. Carlos)

agmacedo@utfpr.edu.br (Andreia G. Macedo)

jaisa@quimica.ufpr.br (Jaísa F. Soares)

ABSTRACT: Seven-coordinate, pentagonal-bipyramidal (PBP) complexes [Ln(bbpen)Cl] and [Ln(bbppn)Cl], in which Ln = Tb^{3+} (products **I** and **II**), Eu^{3+} (**III** and **IV**), and Gd^{3+} (**V** and **VI**), **bbpen**$^{2-}$ = *N,N'*-bis(2-oxidobenzyl)-*N,N'*-bis(pyridin-2-ylmethyl)ethylenediamine, and **bbppn**$^{2-}$ = *N,N'*-bis(2-oxidobenzyl)-*N,N'*-bis(pyridin-2-ylmethyl)-1,2-propanediamine, were synthesized and characterized by single-crystal X-ray diffraction analysis, alternating current magnetic susceptibility measurements, and photoluminescence (steady-state and time-resolved) spectroscopy. Under a static magnetic field of 0.1 T, the Tb^{3+} complexes **I** and **II** revealed single-ion magnet (SIM) behavior. Also, upon excitation at 320 nm at 300 K, **I** and **II** presented very high absolute emission quantum yields (0.90 ± 0.09 and 0.92 ± 0.09 respectively), while the corresponding Eu^{3+} complexes **III** and **IV** showed no photoluminescence. Detailed theoretical calculations on the intramolecular energy transfer (IET) rates for the Tb^{3+} products indicated that both excited singlet and triplet ligand states contribute efficiently to the overall emission performance. The

expressive quantum yields, Q_{Ln}^{L}, measured for **I** and **II** in the solid-state and dichloromethane solution depend on the excitation wavelength, being higher at 272 and 320 nm. Such dependence was rationalized by computing ISC rates (W_{ISC}) and singlet fluorescence lifetimes (τ_S) related to the population dynamics of the S_1 and T_1 levels. Thin films of product **II** showed high air- and photo-stability upon continuous UV illumination, which allowed their use as downshifting layers in a green light-emitting (LED) device. The prototypes presented a luminous efficacy comparable to those found in commercial LED coatings, without requiring encapsulation or dispersion of **II** in host matrices. The results indicate that the PBP environment determined by the ethylenediamine-based ligands investigated in this work favors outstanding optical properties in Tb^{3+} complexes.

Keywords: emission quantum yield • lanthanide • light-emitting device • luminescence • pentagonal-bipyramidal • seven-coordination

INTRODUCTION

Multifunctional lanthanide (Ln)-based materials have been reported in several fields, such as the development of light-emitting and magnetic technologies,[1-4] smart windows,[5-6] and nano-thermometry,[7-9] among others. Luminescent Ln-based complexes have also been used in the selective monitoring of cations in aqueous and biological media[10-13] and cell labeling,[14-16] while complexes with macrocyclic (and other polydentate) ligands have been employed as contrast agents for magnetic resonance imaging (MRI),[17-20] near-infrared probes for bio-imaging and biosensing,[21-22] and study of metabolic reactions at the cellular level.[23] There is huge international demand for such a wide range of applications. Although the total market value of rare-earth raw materials is difficult to estimate because of economic and geopolitical turbulence,[24] industrial end-products containing f-block elements share a global commercial value of several trillion U.S. dollars.[4] Particularly, lanthanide-based phosphors respond for about one-third of this market worldwide.[25-27]

For optical applications, intense efforts have been directed to produce highly luminescent and photostable rare-earth complexes. Magnetic studies, in turn, have focused on the design of molecular Ln-containing systems in which the high magnetic anisotropy leads to record energy barriers to the reversal of magnetization.[28-30] The quest for the strongly desirable combination of magnetic and optical properties in discrete molecules has also motivated synthetic and theoretical studies reviewed recently.[31-32]

The sensitization of trivalent lanthanide (Ln^{3+}) ions via "*antenna* effect" is usually described through the following steps:[27] 1) UV radiation absorption by the ligand, 2) intersystem crossing (ISC) from excited

singlet to triplet states, 3) energy transfer from the ligand triplet state to the Ln^{3+} emitting level and, finally, 4) radiative decay in the visible range. Despite the vast number of publications that establish this singlet→triplet→Ln^{3+} pathway as the main energy transfer mechanism in highly luminescent Ln^{3+} complexes, the importance of alternative singlet→Ln^{3+} routes have also been recognized,[27, 33] after being considered less important for many years. The frequency of reports on more than one relevant donor state, or a dominant singlet energy transfer, has increased significantly, and several systems are now well-characterized.[34-44]

Improvement of the absorption/energy transfer processes to give luminescent materials with long decay times and high absolute emission quantum yields (the ratio between the number of emitted photons by the lanthanide and the absorbed photons by the ligands, Q_{Ln}^{L})[45] is an extensively sought task, to which the design of ligands with specific coordination geometries and the use of different counterions have contributed significantly.[46-49] In this context, we recently reported the preparation of two eight-coordinate Tb^{3+} nitrates with the polydentate ligands *N,N'*-bis(2-oxidobenzyl)-*N,N'*-bis(pyridin-2-ylmethyl)-ethylenediamine (**bbpen**$^{2-}$) and *N,N'*-bis(2-oxidobenzyl)-*N,N'*-bis(pyridin-2-ylmethyl)-1,2-propane-diamine (**bbppn**$^{2-}$), which present significantly different Q_{Ln}^{L} values of *ca.* 0.21 and 0.67 respectively.[50] In these compounds, thermally active non-radiative pathways are available for [Tb(bbpen)(NO_3)], and respond for excited-state deactivation processes, but, on the contrary, are minimized in the **bbppn**$^{2-}$ analog. The differences in the optical properties of the two compounds relate to the conformation of the ethylenediamine (en) bridge in the ligand, the distorted dodecahedral coordination geometry about the chelated Tb^{3+} ion, and differing packing pressures in the solid state.[50]

Structural changes in the ligand backbone and their effect on the quantum yield of Tb^{3+} complexes, in this case with 2,2'-bipyridine (bipy) derivatives, were theoretically assessed by M. Hatanaka *et al.*.[48] By comparing ligands with different bridging groups connecting the bipy rings, they found that the barrier for the deactivating ISC from triplet to (fundamental) singlet increases when the motions that induce the ISC are restrained. This situation favors energy transfer to the $^5D_4$ emitting level of Tb^{3+}. The substitution of counter ions, in turn, impacts the emission quantum yields and monochromaticity because it modifies coordination number and geometry, organic ligand conformation, crystal packing, and molecular/crystal symmetry. This behavior has been reported, for instance, for Tb^{3+} complexes with *N*-substituted tris(benzimidazol-2-ylmethyl)amine (ntb) and several different anions (NO_3^-, Cl^-, ClO_4^-, $CF_3SO_3^-$, and picrate).[51] The distinct coordination abilities of these counterions led to clearly distinguishable photophysical properties by affecting site symmetry and tuning the triplet energies of the ligands.[51]

In the present work, we report luminescence measurements for [Ln(**bbpen**)Cl] and [Ln(**bbppn**)Cl] complexes **I** to **IV** (Ln = Tb^{3+} and Eu^{3+}), comparing the results with those obtained for the corresponding Tb^{3+} compounds with chelating NO_3^- ligands.[50] The deceptively simple replacement of bidentate NO_3^- with monodentate Cl^- results in drastic geometry change from distorted dodecahedral to pentagonal-bipyramidal (PBP), and a remarkable increase in Q_{Ln}^L for both Tb^{3+} complexes. Interestingly, a very recent review on the low symmetry of seven-coordinate Ln^{3+} environments, and its possible effect on photophysical properties, has been published.[52] It focuses mostly on β-diketonate-based complexes, but its findings reinforce the importance of a thorough investigation of the possible generality of such structure-luminescence correlations. In the present work, we also carried out Density Functional Theory (DFT) and Intramolecular Energy Transfer (IET) calculations to rationalize the relationship between energy levels and transfer rates in complexes **I** and **II**, and subsequently clarify which factors, related to the pentagonal-bipyramidal coordination of Ln^{3+} ions, contribute more to the observed enhancement of the optical properties.

The PBP geometry is also distinctive in favoring very high magnetic anisotropy in Dy^{3+} complexes such as [Dy(bbpen)X][53] and its methylated derivative [Dy(bbpen-Me)X],[54] X = chloride or bromide. For these compounds, effective barriers to magnetic relaxation equal to or higher than 1000 K were reported as record values, being still among the highest ones described to date. To the best of our knowledge, on the other hand, the dynamics of the magnetic susceptibility of Tb^{3+} complexes with distorted pentagonal-bipyramidal geometry has not been investigated. For these reasons, we also measured the alternating current (AC) magnetic susceptibility of products **I** and **II**, which contain Tb^{3+} ion instead of Dy^{3+},[53-54] to add information on electronic factors that influence magnetic relaxation in mononuclear lanthanide complexes with PBP geometry.

The results reported hereafter reinforce the sensitivity of the luminescence and magnetic properties of Ln^{3+} complexes to the geometric constraints imposed by the chelating ligands, and provide a high-performance example of combined excited-singlet- and excited-triplet-to-Ln^{3+} IET mechanisms. They also, and importantly, highlight the striking suitableness of ethylenediamine-based mixed-donor ligands as optical sensitizers for Tb^{3+} as compared to Eu^{3+} ions. Moreover, the air- and photo-stability of complexes **I** and **II**, combined with the remarkably significant quantum yields, allow the fabrication of pure molecule-based LEDs comparable to high-performance mixed-oxides reported in the literature. The precise synthetic control, reproducible preparation, and fine structural tuning open a promising way to using this class of chelating compounds in the development of new and efficient optical devices.

EXPERIMENTAL SECTION

General

Chemicals were purchased from Sigma-Aldrich and used as received. Solvents (Honeywell/Riedel-de Haën, Vetec, Aldrich) were dried by standard methods[55] and distilled under N_2 before use. The proligands **H_2bbpen** and **H_2bbppn** were prepared according to previous reports.[56-57] The solvent (CH_2Cl_2) employed in LED fabrication and electronic spectroscopy was dried over activated 3 Å molecular sieves for 48 h before use. Carbon, hydrogen, and nitrogen (combustion) analyses were run by MEDAC Laboratories Ltd. (Chobham, Surrey, U.K.) or by the Analytical Center of the University of São Paulo (USP, Brazil), on a Thermal Scientific Flash ES 1112 series Elemental Analyzer or a Perkin Elmer 2400 Series II equipment respectively. FTIR spectra were registered in KBr pellets on BIORAD FTS 3500GX or BOMEN Michelson MB100 spectrophotometers. UV/Vis reflectance spectra and absorption spectra in dichloromethane solution were acquired on a PerkinElmer LAMBDA 1050 UV/Vis/NIR spectrophotometer equipped with a PMT/InGaAs/PbS three-detector setup.

Syntheses of Complexes I-VI

The $LnCl_3{\cdot}6H_2O$ starting materials (Ln = Tb^{3+}, Eu^{3+} or Gd^{3+}) were dissolved in methanol and allowed to react under N_2 with **H_2bbpen** or **H_2bbppn** in the presence of stoichiometric amount of trimethylamine; the procedure was adapted from that described by Yamada and co-workers for other Ln^{3+} ions.[58] Single crystals suitable for X-ray diffraction analysis were grown from the mother liquor or from dichloromethane solutions upon slow liquid or vapor diffusion with diethyl ether, tetrahydrofuran or glyme. Crystals were light pink for Tb^{3+}, colorless for Gd^{3+}, and yellow or gold-yellow for Eu^{3+}. Yields ranged from 40 to 85% and were typically higher for **$bbpen^{2-}$** than for **$bbppn^{2-}$** complexes, due to solubility differences. Crystalline **I**-**VI** are air-stable and were therefore manipulated and characterized in air.

Anal. calcd for $C_{28}H_{28}ClN_4O_2Tb$ (**I**): C, 51.98; H, 4.36; N, 8.66. Found: C, 51.75; H, 4.43; N, 8.62.

Anal. calcd for $C_{29}H_{30}ClN_4O_2Tb$ (**II**): C, 52.70; H, 4.57; N, 8.48. Found: C, 52.52; H, 4.35; N, 8.41.

Anal. calcd for $C_{28}H_{28}ClEuN_4O_2$ (**III**): C, 52.55; H, 4.41; N, 8.75. Found: C, 52.57; H, 4.44; N, 9.46.

Anal. calcd for $C_{29}H_{30}ClEuN_4O_2$ (**IV**): C, 53.26; H, 4.62; N, 8.57. Found: C, 52.89; H, 5.02; N, 8.63.

Anal. calcd for $C_{28}H_{28}ClGdN_4O_2$ (**V**): C, 52.12; H, 4.37; N, 8.68. Found: C, 52.00; H, 4.41; N, 8.57.

Anal. calcd for $C_{29}H_{30}ClGdN_4O_2$ (**VI**): C, 52.83; H, 4.59; N, 8.50. Found: C, 52.63; H, 4.29; N, 8.32.

Single-Crystal X-Ray Structural Analysis

Diffraction data for complexes **I-VI** were collected on a Bruker D8 Venture diffractometer equipped with a Photon 100 CMOS detector, a Mo–Kα radiation source, and a graphite monochromator. Crystals were mounted on MiTeGen® micromeshes. Intensity data were measured by thin-slice ω- and ϕ-scans at a fixed temperature, for each compound, between 274(2) and 302(2) K (see Table S1). Data were processed using the Bruker APEX3 software.[59] Structures were determined by the intrinsic phasing routines in the SHELXT program[60] and refined by full-matrix least-squares methods, on F^2's, in SHELXL.[61] All non-hydrogen atoms were refined with anisotropic thermal parameters; hydrogen atoms were included in idealized positions, and their U_{iso} values were set to ride on the U_{eq} values of the parent carbon atoms. Scattering factors for neutral atoms were taken from the literature.[62] All computer programs used in these analyses were run through WinGX[63-64] at the Universidade Federal do Paraná and the University of East Anglia. Crystal data, data collection, and general structure refinement data are presented in Table S1. Crystal and molecular drawings in the main text and Supplementary Information were made with the Diamond software.[65]

Photoluminescence and Photostability Measurements

Emission and excitation spectra were recorded with the front face acquisition mode at both 11 and 300 K on a Fluorolog®–3 (Model FL3-2T, Horiba Scientific) with modular double grating excitation (1200 grooves/mm, blazed at 330 nm), fitted with a TRIAX 320 single-emission monochromator (1200 grooves/mm, blazed at 500 nm, reciprocal linear density of 2.6 nm mm^{-1}) coupled to an R928 Hamamatsu photomultiplier. The excitation source was a 450W Xe arc lamp. The emission spectra were corrected for detection and optical spectral response of the spectrofluorimeter, while the excitation spectra were corrected for the spectral distribution of the lamp intensity using a photodiode reference detector. Time-resolved measurements were carried out with the setup described for the luminescence spectra using a pulsed Xe-Hg lamp (6×10^{-6} sec pulse at half-width and $20\text{-}30\times10^{-6}$ sec tail). For photoluminescence measurements, all samples were processed in pellets with 0.5 mm thickness.

Photo-stability measurements were performed by using UV LEDs (325 or 365 nm) as excitation sources. The UV light was guided by an optical fiber near the surface of the Tb^{3+} pellets; the green emission was then collected by another optical fiber and directed to a Maya portable spectrometer (Ocean Optics). These measurements were performed in air at room temperature. The stability of the fabricated LED was evaluated in the Fluorolog®–3.

Absolute Emission Quantum Yields

The absolute emission quantum yields were measured at room temperature using the Quantaurus-QY Plus UV-NIR absolute PL quantum yield spectrometer (C13534-31, Hamamatsu) with a 150 W Xenon lamp as the excitation source and two detectors (BT-CCD, 300-950 nm, and InGaAs, 900-1650 nm, see Table S16). Three measurements were made for each sample so that the average value is reported. The method is accurate within 10% of the measured values.

Production of a Downshifting Layer for Light-Emitting Devices (LED)

The prototypes consisted of commercial near-UV-emitting LED chips (365±10 nm, surface mounted diode (SMD) type, Shenzhen Chang Long Technology Co.) covered with complex **II** previously stirred in dichloromethane (5.0 mg mL^{-1}; 7.6 mmol L^{-1}) for 10 min at room temperature. The resulting clear and colorless solution was drop-cast (10 µL) on the commercial UV-LED chip forming a coating layer. The solvent was removed by drying in air at room temperature. This deposition and drying procedure was repeated several times to afford the homogeneous thin films. The reproducibility was confirmed by fabricating two different LED prototypes. The deposition of the luminescent layer was performed by the remote method, meaning that the film was coated on the cap of the LEDs, not on the PN junction. This procedure avoids the exposition of the luminescent coating to the temperature of the PN junction,[66] and the break of the junction by the solvents.

The luminous flux of the LED prototypes was measured using an integrating sphere ($BaSO_4$ coating; internal diameter 150 mm, ISP 150L-131, Instrument Systems) coupled to a MAS 40 array spectrometer. According to the manufacturer, the measurements are accurate to within 5%. The voltage and current on the LED prototipes were measured using a SourceMeter (2400 SMU Instruments, Keithley) and the the luminous efficacy (η) values were calculated (η = luminous flux/ electric power).

The emission stability of the prototypes was monitored for 10.5 h of operation at 3.2 V, Figure S19b, using the Fluorolog®–3.

Alternating Current (AC) Magnetic Susceptibility Measurements

Samples employed for AC magnetic susceptibility measurements consisted of microcrystalline powders of products **I** and **II** pressed into pellets and wrapped in Teflon tape. AC magnetic susceptibility analyses were performed on a Quantum Design PPMS (Physical Properties Measurement System) platform, with oscillating field frequencies ranging from 10 to 10000 Hz, and using a static magnetic field of 0.1 T. The resulting magnetic data were corrected for the diamagnetic contributions of the samples, calculated from Pascal constants,[67] together with those measured for the sample holder, and wrapping

Teflon tape. Susceptibility data were analyzed with the extended Debye model[68-69] as described in the Supporting Information (Eq. S1 and figures therein).

THEORETICAL SECTION

In Silico Experiments

The geometry optimization calculations were performed at the B3LYP[70-71] level using the 6-311++G(d,p)[72-74] basis set for hydrogen, carbon, nitrogen, and oxygen atoms, while the core potential MWB52 was used, with its associated valence basis set, for the lanthanide ions.[75] The overlap integrals (ρ) were calculated using the BP86/STO-TZ2P method within the ADF program.[76-77] The excitation energies of the complexes were calculated using time-dependent density functional theory (TD-DFT) at the same level of theory (B3LYP/MWB52(Eu)/6-311++G(d,p)) employed in the geometry optimization procedure.

Energy Transfer Rates

Intramolecular energy transfer (IET) rates were calculated taking into account the dipole-dipole (W_{d-d}), dipole-multipole (W_{d-m}), and exchange (W_{ex}) mechanisms operating in coordination compounds, according to Eqs. 3–5.[78-81] These calculations, aside from allowing quantitative estimates of energy transfer rates, also lead to selection rules of paramount importance in interpreting experimental results.

Estimates of the energy transfer rates were obtained from the following expressions for dipole-multipole contributions, in which $K = 2, 4,$ and 6:

$$W_{d-m} = \frac{S_L}{(2J+1)G}\frac{2\pi e^2}{\hbar}\sum_K (K+1)\frac{\langle r^K\rangle^2}{(R_L^{K+2})^2}\langle f\|C^{(K)}\|f\rangle^2(1-\sigma_K)^2\langle\psi^*J^*\|U^{(K)}\|\psi J\rangle^2 F \quad (1)$$

The dipole-dipole contribution can be estimated using:

$$W_{d-d} = \frac{S_L(1-\sigma_1)^2}{(2J+1)G}\frac{4\pi}{\hbar}\frac{e^2}{R_L^6}\sum_K \Omega_K^{FED}\langle\psi^*J^*\|U^{(K)}\|\psi J\rangle^2 F \quad (2)$$

where the intensity parameters Ω_K^{FED} are calculated by Eq. S4 using only the Forced Electric Dipole (FED, Eq. S5) contribution (with Simple Overlap Model[82-83] or other ligand field models).

The exchange mechanism, which is very sensitive to short-range interactions, is calculated as:[84]

$$W_{ex} = \frac{(1-\sigma_0)^2}{(2J+1)G}\frac{8\pi}{3\hbar}\frac{e^2}{R_L^4}\langle\psi^* J^* \| S \| \psi J\rangle^2 \sum_m \left| \left\langle \phi \left| \sum_j \mu_z(j) s_m(j) \right| \phi^* \right\rangle \right|^2 F \quad (3)$$

In Eqs. 1-3, the F parameter is the spectral overlap factor, which contains the energy mismatch condition between donor and acceptor states.[78, 82] In the case of energy transfer involving lanthanide complexes, the F value can be obtained by:

$$F = \frac{1}{\hbar\gamma_L}\sqrt{\frac{ln(2)}{\pi}}\, e^{-\left(\frac{\Delta}{\hbar\gamma_L}\right)^2 ln(2)} \quad (4)$$

Eq. 4 can be assumed only when the bandwidth at half-height for the donor state of the ligand (γ_L) is much larger than the acceptor state of the lanthanide (γ_{Ln}) ion, $\gamma_L \gg \gamma_{Ln}$.[85] The energy difference between the donor-acceptor states is given by $\Delta = E_L - E_{Ln}$.[82, 86]

RESULTS AND DISCUSSION

Synthesis and Structural Characterization by Single-Crystal X-Ray Diffraction Analysis

Products **I**-**VI** crystallize in good yields without coordinating or solvating water molecules, despite being produced from hydrated Ln^{3+} chlorides. A comparison of their FTIR spectra is presented in Figure S1. Their air-stability proved to be a very convenient feature as far as the magnetic and photoluminescence studies described in this work are concerned.

The three complexes obtained with **bbpen^{2-}**, namely products **I** (Tb), **III** (Eu), and **V** (Gd), are isostructural in the crystalline state (orthorhombic *C*222$_1$ space group). Compounds that contain **bbppn^{2-}** (**II**, **IV,** and **VI**), in turn, are also isostructural and crystallize in the *C*2/*c* (monoclinic) space group. Figure 1 represents the molecular structures of **I** and **II**, with corresponding drawings for compounds **III**-**VI** given in Figures S2 and S3. Experimental details on data collection and refinement for all products are presented in Table S1, while selected bond lengths and angles discussed in the text appear in Table 1. A complete list of molecular dimensions is available in the **Supporting Information** (Tables S2–S7), together with representative packing diagrams in Figure S4.

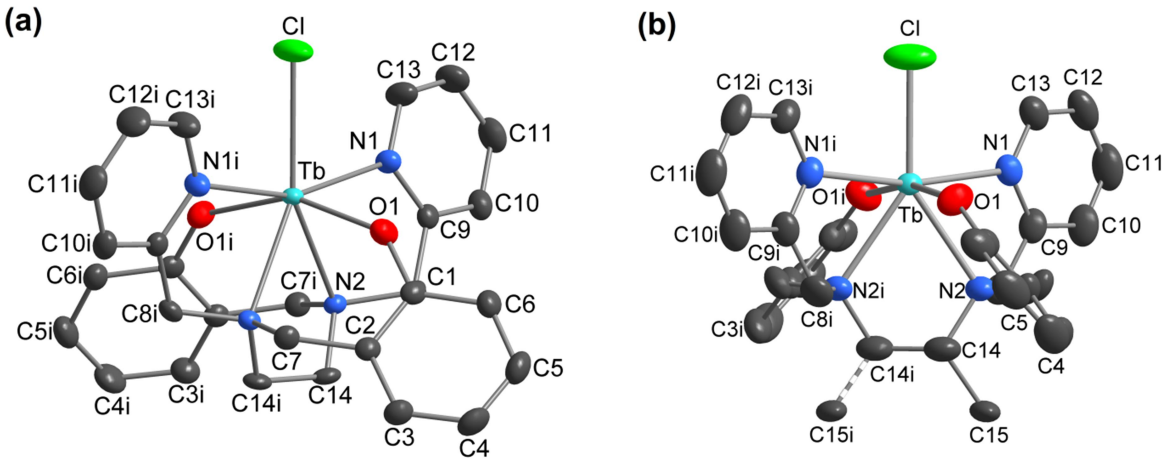

Figure 1. Representations of the molecular structures of complexes **I** (a), [Tb(bbpen)Cl], and **II** (b), [Tb(bbppn)Cl], with the atom numbering scheme. In the diagram of **II**, the two disordered orientations of the C(15) atom are distinguished by solid and dashed bonds.

Table 1. Selected bond lengths (Å) and angles (°) for complexes **I**-**VI**, [Ln(bbpYn)Cl] (Y = e, p), with estimated standard deviations in parentheses. The symmetry operations #1, #2 and #3 are -x, y, 1/2-z; 2-x, y, 3/2-z; and 1-x, y, 3/2-z respectively

[Ln(bbpen)Cl]					
Complex **I**		Complex **III**		Complex **V**	
Tb-O(1)	2.176(2)	Eu-O(1)	2.1994(17)	Gd-O(1)	2.1963(17)
Tb-N(1)	2.575(3)	Eu-N(1)	2.595(2)	Gd-N(1)	2.585(2)
Tb-N(2)	2.597(2)	Eu-N(2)	2.6230(19)	Gd-N(2)	2.609(2)
Tb-Cl	2.6805(9)	Eu-Cl	2.7083(7)	Gd-Cl	2.6934(7)
O(1)#1-Tb-O(1)	153.68(11)	O(1)-Eu-O(1)#2	152.27(9)	O(1)#1-Gd-O(1)	152.72(9)
[Ln(bbppn)Cl]					
Complex **II**		Complex **IV**		Complex **VI**	
Tb-O(1)	2.187(2)	Eu-O(1)	2.196(4)	Gd-O(1)	2.206(2)
Tb-N(1)	2.560(3)	Eu-N(1)	2.597(5)	Gd-N(1)	2.572(3)
Tb-N(2)	2.596(3)	Eu-N(2)	2.626(5)	Gd-N(2)	2.605(3)
Tb-Cl	2.5971(15)	Eu-Cl	2.633(2)	Gd-Cl	2.6086(13)
O(1)-Tb-O(1)#3	165.83(13)	O(1)-Eu-O(1)#3	165.8(2)	O(1)-Gd-O(1)#3	165.66(12)

Molecules of **I**-**VI** adopt distorted PBP geometry as exemplified in Figure 2 for complex **V**. A similar arrangement of the donor atoms has also been reported by Yamada *et al.*[58] for [Ln(bbppn)X], with Ln = Lu^{3+}, Yb^{3+} and X = Cl^-, SCN^-; by Liu *et al.*[53] for [Ln(bbpen)X], Ln = Dy^{3+}, Y^{3+}; and by Jiang *et al.*[54] for [Dy(bbpen-Me)X]. In the last two cases, X = Cl^- and Br^-. Based on the available literature data and the results described in this work, we find that, in this class of seven-coordinate species, the departure from the ideal PBP dimensions can be measured by *(i)* $\Delta L_{equat(max)}$, or the maximum bond length difference in the equatorial plane; *(ii)* the maximum distance between the equatorial atoms and the mean (calculated) pentagonal plane, $\Delta D_{plane(max)}$; and *(iii)* the deviation from 180° of the bond angle involving the axial (oxygen) atoms, ΔA_{axial}. These values are presented in Table 2 and evidence how structurally disturbing is the insertion of C(15) upon the planarity of the equatorial donor atoms in the **bbppn**$^{2-}$ complexes (high

$\Delta\underline{D}_{plane(max)}$), but, on the other hand, how this same insertion decreases the disparity in bond lengths in the pentagonal plane (low $\Delta\underline{L}_{equat(max)}$) and also leads to a more axial structure, as far as the O(1)–Ln–O(1^{i}) angle is concerned (small $\Delta\underline{A}_{axial}$). Such close-to-axial symmetry involving the strongly donating phenoxide groups may contribute to increased magnetic anisotropy depending on the prolate or oblate nature of the central lanthanide ion.[53-54]

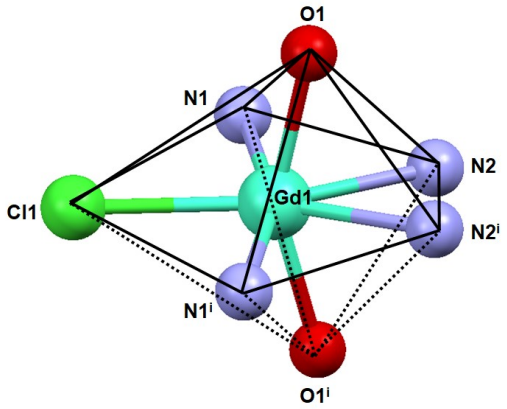

Figure 2. Distorted pentagonal-bipyramidal coordination sphere of the metal ion in [Gd(bbpen)Cl] (complex **V**).

Table 2. Structural deviation from ideal PBP geometry in complexes **I-VI** ([a])

Complex	Ligand	$\Delta\underline{L}_{equat\ (max)}$ (Å)	$\Delta\underline{D}_{plane\ (max)}$ (Å) [b]	$\Delta\underline{A}_{axial}$ (°)
I (Tb)	bbpen^{2-}	0.106	0.221	26.3
III (Eu)		0.113	0.228	27.7
V (Gd)		0.108	0.225	27.3
II (Tb)	bbppn^{2-}	0.037	0.568	14.2
IV (Eu)		0.037	0.568	14.2
VI (Gd)		0.037	0.586	14.4

([a]) Parameters determined with the Mercury software.[87] For the meaning of $\Delta\underline{L}$, $\Delta\underline{D}$ and $\Delta\underline{A}$, see text. ([b]) The distance from the mean plane was measured from N(2) or N(2^{i}).

The two types of crystal structure, represented by the non-centrosymmetric $C222_1$ and the centrosymmetric $C2/c$ space groups, also differ in crystal chirality. Accordingly, although the individual molecules of **II**, **IV**, and **VI** present *N*-, *C*- (*R* or *S*), and metal-centered chirality (Δ *versus* Λ),[50, 58] the inversion centers in the $C2/c$ unit cell prevent the existence of enantiomeric crystals. On the other hand, the Sohncke space group[88-89] $C222_1$ displays only rotations, translations, and rototranslations in the unit cell, opening the possibility of chiral crystal structures for the **bbpen^{2-}** complexes **I**, **III**, and **V** (Flack parameter[88] of -0.005(5) for **I**, for example). However, such structural distinction does not seem to differentiate the magnetic or light-emitting properties of the Tb^{3+} and Eu^{3+} compounds **I**-**IV** (see below).

Despite the different temperatures of data collection, the comparison of selected crystallographic data obtained for [Tb(bbpen)X] and [Tb(bbppn)X], X = Cl^{-} or NO_3^{-},[50, 90] indicates a few consistent general trends (Tables S8 and S9). Firstly, when X is changed, the resulting bond lengths around the lanthanide

ion (Tb–$O_{phenoxide}$, Tb–N_{amine}, Tb–N_{py}, and Tb–X) change more with **bbpen**$^{2-}$ (Table S8) than with **bbppn**$^{2-}$ (Table S9). This may suggest that **bbpen**$^{2-}$ generates a more flexible coordination geometry that is especially sensitive to steric demands of the anionic coligand. This observation is in line with the fact that when confronting the two nitrate complexes, the one with **bbpen**$^{2-}$ presents a much lower quantum yield (21 ± 2 %) than its **bbppn**$^{2-}$ analog (67 ± 7%), a result attributed to a more rigid environment created by **bbppn**$^{2-}$.[50] Accordingly, the disparity in bond lengths in the coordination polygon of the Tb^{3+} chlorides is again larger with **bbpen**$^{2-}$, as already shown in Table 2 by the $\Delta L_{equat(max)}$ parameter.

The two most striking structural observations for the Tb^{3+} halide complexes here described (complexes **I** and **II**) are the decrease in the Ln–Cl bond length, from 2.6805(9) to 2.5971(15) Å, and the dramatic increase in the $O_{phenoxide}$–Tb–$O_{phenoxide}$ angle from 153.68(11)° to 165.83(13)° when replacing **bbpen**$^{2-}$ with **bbppn**$^{2-}$ (Table 1). These specific differences do not significantly affect the optical properties of complexes **I** and **II**, shown in the next sections to be excellent in both cases. This suggests that the PBP geometry, differently from the distorted dodecahedron of the nitrate complexes,[50, 90] may be a compact environment that enhances the *antenna* effect of these ethylenediamine-based ligands and prevents the deactivation of the emitting levels. Thus, the considerably better photophysical performance of the chloride-containing [Tb(bbp**Y**n)Cl] (Y = e, p) products as compared to their NO_3^- analogs[50] appears to be determined by the PBP environment of the Ln^{3+} ions in the individual molecules and by their electronic structure, rather than by the presence or absence of crystal chirality. This proposition on the suitability of the PBP geometry is supported by a recent work by Ayers and co-workers in which the related **tpen** ligand (tetrakis(2-pyridylmethyl)ethylenediamine) generates an eight-coordinate square-antiprismatic coordination sphere for the Tb^{3+} ion; the complex presents a quantum yield of 55.3 % in the solid-state.[91] This value is significantly lower than those for PBP [Tb(bbp**Y**n)Cl] (Y = e, p; this work) and close to the result given by eight-coordinate [Tb(bbppn)(NO_3)].[50, 90]

From the magnetic point of view, the structural differences reported above between complexes with **bbpen**$^{2-}$ or **bbppn**$^{2-}$ also do not significantly affect the relaxation dynamics of **I** and **II**, which are very similar. In fact, both our sets of data (magnetic and optical) suggest the adoption of the PBP geometry to override subtle structural differences in the ligands and be itself a determining factor in Tb^{3+} properties. These findings differ from the photophysical results for Tb^{3+} complexes with the same ligands in a distorted dodecahedral coordination environment.[50]

Magnetization Dynamics

The magnetization dynamics of complexes **I** and **II** was investigated by AC susceptometry on polycrystalline samples. The isothermal field dependences of magnetic susceptibility of both samples,

measured at 2.0 K, are reported in Figure S5, and show no out-of-phase χ_M" in zero field, in striking contrast with what was observed for Dy^{3+} analogs.[53-54] Upon application of a static field of 1 kOe, in turn, both **I** and **II** display frequency- and temperature-dependent magnetic behavior typical of single-ion magnets (SIM). Accordingly, Figure 3(a) shows peaks in the χ_M"(ω) curves whose maxima shift to higher temperatures upon increasing oscillation frequency of the field. Products **I** and **II** present strikingly similar temperature χ_M"(ω) dependences (Figure S6). Such a finding suggests that, for these Tb^{3+} chloride complexes in the PBP coordination environment, the effect of inserting one additional methyl group in the **bbppn**$^{2-}$ complex **II** *versus* its absence in **I** is not as determining of molecular properties (apart from structural) as it was for the eight-coordinate analogs with coordinated NO_3^-.[50] This result parallels most of the optical properties of the two chloride-containing complexes described in the next sections.

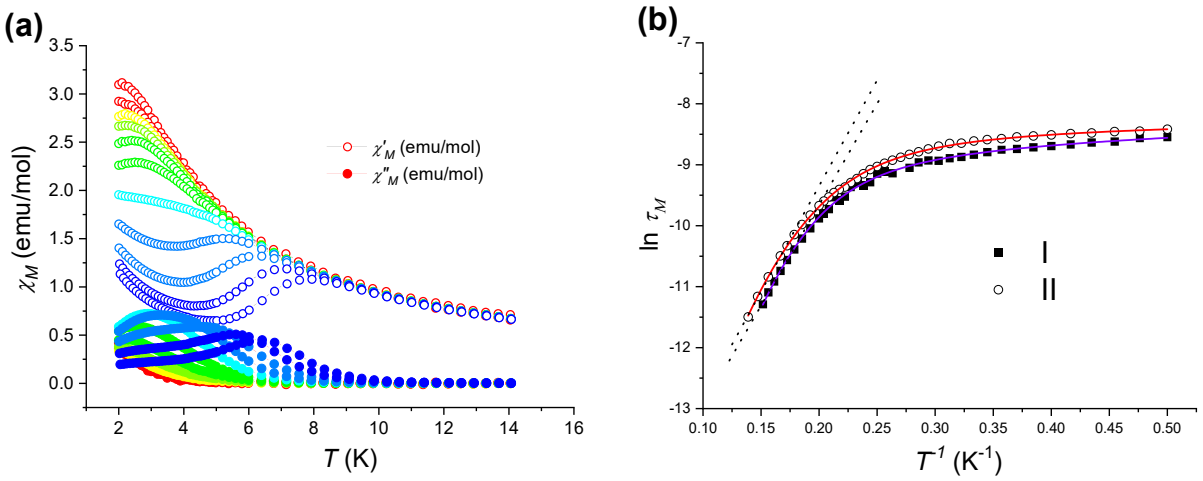

Figure 3. (a) Temperature dependence of χ_M' and χ_M" for complex **II**, measured with a static field of 1.0 kOe for eleven logarithmically-spaced frequencies of the oscillating field, spanning the range between 10 Hz (red data) and 10 kHz (blue data). (b) Temperature dependence of the magnetic relaxation times, τ_M, extracted from AC susceptibility data measured for **I** and **II**, reported as an Arrhenius plot.

Fitting of the isothermal χ_M"(ω) curves allowed to extrapolate the magnetic relaxation times (τ_M) of **I** and **II** at different temperatures. These parameters are reported in the Arrhenius plot of Figure 3(b). To fit the plots for both compounds, a relaxation model involving three different processes has been used, as described by:

$$\frac{1}{\tau} = CT^n + AT + \nu_{QTM} \qquad (5)$$

In this model, the first term describes the relaxation of the molecular magnetization through a Raman process, the second a direct relaxation between two magnetic states, and the third term, the quantum tunneling of the magnetization between degenerate $\pm m_J$ states.[92] The parameters obtained from the fit

are reported in Table S10. It must be stressed that, even though our measurements were performed in the presence of a static field, the last term (ν_{QTM}) was necessary to reproduce satisfactorily the low-temperature range of the plots. We attribute this behavior to the non-Kramers nature of the Tb^{3+} ion, similarly to what was observed for other Tb^{3+} SIMs, which activates efficient mixing between states belonging to different sides of the double potential energy well.[93-95] The values obtained for the *n* exponent of the Raman process are 6.9(2) for **I** and 6.06(7) for **II**, in line with the value of 7 expected for a non-Kramers ion,[96] and differing, as expected, from the lower values encountered in a recent study with the Gd^{3+} complex **V**, [Gd(bbpen)Cl].[97] The α parameter in Eq. S1, whose maximum values are 0.29 and 0.26 for **I** and **II** respectively at 2.0 K (Figure S7), indicates a narrow distribution of relaxation times. Attempts to fit the plots using a mixed approach involving an Orbach relaxation mechanism yielded poorer results and were discarded.[98] For comparison with previous reports from the literature, an evaluation of the effective barrier to the thermally-activated magnetic relaxation has been carried out by fitting the T > 5.8 K data with an Arrhenius function, yielding the values of 23(1) and 24(1) cm^{-1} for **I** and **II**, respectively. Even if the unambiguous determination of the magnetic relaxation pathway in the Tb^{3+} complexes **I** and **II** would require a more thorough spectroscopic and theoretical analysis that is beyond the scope of the present manuscript, our results here indicate that a mixed Raman/direct/QTM mechanism is likely to be active for both compounds. This proposal is reinforced by the fact that the energy differences involving the m_J states of the ground $^7F_6$ multiplet in complexes **I** and **II** (as extracted from the emission spectra in Figure S12b), being in the 60-100 cm^{-1} range, are not compatible with the relaxation barriers determined from Figure 3b for an Orbach relaxation mechanism.

The non-Kramers nature of the Tb^{3+} ion seems to be decisive to give fast relaxation in zero field and provide SIM behavior only upon applying a low-intensity static field, differently from the observed for the Dy^{3+} analogs,[53-54] and overruling the structural differences between **I** and **II**. This trend has been associated to spin-parity effects.[95] On the other hand, several examples of eight-coordinate Tb^{3+} compounds with capped- or pseudo-square antiprism coordination reported in the literature failed to display slow relaxation of the magnetization even in the presence of an applied magnetic field,[93-95] while the PBP systems investigated herein clearly display slow magnetization dynamics in such conditions (static field 1 kOe). These results indicate that the distorted pentagonal-bipyramidal geometry of the crystal field in **I** and **II** may hold promise to reduce the through-barrier mixing of the $\pm m_J$ sublevels of the Tb^{3+} ground state, and effectively promote the desirable zero-field SIM behavior in this integer J system.

Excited States for Complexes I and II

The UV-visible diffuse reflectance spectra of the Tb^{3+} complexes **I** (with **bbpen**$^{2-}$) and **II** (**bbppn**$^{2-}$) in the solid-state present broad and intense, overlapping bands below 400 nm, together with a prominent shoulder at 425-550 nm, Figure S8. This energy absorption profile is well compatible with a potential *antenna* effect. The assignment of selected excitations and the possibility of ligand-to-metal charge transfer (LMCT) bands close to the donor states were investigated by Time-Dependent Density Functional Theory (TD–DFT) calculations (see *In silico experiments*). LMCT transitions were not observed in the first 100 excitations (from 406 to 240 nm), indicating that, in complexes **I** and **II**, LMCT states probably have high energies with corresponding wavelengths shorter than 240 nm. More details are given as Supplementary Information (*Calculated MO Energy Diagrams and Composition of Selected Excitations,* and Figures S20-S22).

Diffuse reflectance and emission spectra were also acquired for the Gd^{3+} complexes **V**, [Gd(bbpen)Cl)], and **VI**, [Gd(bbppn)Cl], to assess the ligand singlet and triplet energy levels. The lowest-energy excited singlet state (S_1) was observed at *ca.* 27000 cm^{-1} (370 nm), Figures S9a and S10a. The singlet energies were estimated from the reflectance spectra acquired from the Gd^{3+} complexes **V** and **VI** (Figures S9a and S10a), which were deconvoluted in Gaussian bands with maxima at *ca.* 37050 cm^{-1} (270 $\pm$ 25 nm), *ca.* 31650 cm^{-1} (316 $\pm$ 25 nm), and *ca.* 27000 cm^{-1} (370 $\pm$ 20 nm). These values are in good accordance with the results of theoretical calculations, as presented below and in Figures S21 and S22.

Time-resolved emission spectra registered at 11 K are shown in Figures S10b and S11. The emission in the 440–600 nm region arises mainly from triplet manifolds, as confirmed by the long decay times of 0.710 ± 0.017 ms (monitored at 440 and 500 nm) and 0.925 ± 0.016 ms (monitored at 540 nm) measured upon wavelength excitation at 325 nm. Moreover, by increasing the excitation wavelength to 365 or 385 nm, similar bands were observed, but with variations in relative intensities, Figure S10b. This change in excitation wavelength allowed us to search for different components of the triplet emission prior to the determination of the band barycenter and zero-phonon line (Figure S11). The zero-phonon energy is observed around 25100 cm^{-1} (*ca.* 400 nm), in accordance with the theoretical TD-DFT result (Figures S21 and S22).

The triplet bands shown in Figure S10b occur in the same energy region of the time-resolved emission spectra recorded for the **H_2bbppn** pro-ligand, Figure S10d. In the case of the proligand, the triplet decay times are much longer (*ca.* 120 ms for λ_{em}= 440 nm and λ_{exc}= 310 nm at 11 K), as expected in the absence of a heavy atom,[99] when compared with the values registered for products **V** and **VI**.

For both Gd^{3+} complexes, the experimentally observed S_1 state at *ca.* 27000 cm^{-1} is approximately 6000 cm^{-1} above the triplet band with barycenter at *ca.* 21000 cm^{-1} (about 475 nm, Figure S11). Such difference, smaller than 7000 cm^{-1}, favors intersystem crossing (ISC) to the triplet over competitive relaxation back to the ground (S_0) state.[100] On the other hand, the energy difference between the barycenter of the triplet band and the $^5D_4$ level of Tb^{3+} (20400 cm^{-1}) is small (*ca.* 600 cm^{-1}), suggesting the possibility of back-transfer between these states; this was considered in the theoretical modeling discussed in the following section. Also, in complexes **I** and **II**, the relative energies of the excited ligand states and the Tb^{3+} levels are compatible with the direct energy transfer from S_n (n = 1-3). This agrees with the operation of additional singlet pathways,[27, 40, 42-44] as discussed below.

Excitation and emission spectra measured at 11 K are presented in Figure S12. Complex **II** presents longer $^5D_4$ decay times (τ_4), both at room temperature and 11 K, compared with **I** (Table 3 and Figure S13). This result is probably due to the effect of the methyl groups attached to C(14) (see Figure 1) in **II**, which apparently deactivates vibrational modes that lead to a shorter lifetime in **I**. Despite this difference, both complexes present very high Q_{Ln}^L values, as also indicated in Table 3. To the best of our knowledge, the absolute quantum yields of *ca.* 0.9 measured for **I** and **II** are among the highest values reported for Tb^{3+} complexes to date,[52, 101-106] nearing quantitative yields. These results, and the air-stability of the compounds, prompted us to investigate their performance in optoelectronic devices that require high luminescence in the ambient atmosphere, as described in the next sections.

Table 3. Room temperature and 11 K $^5D_4$ lifetimes (τ_4), monitored at λ_{em} = 540.5 nm, and absolute emission quantum yields[27, 107] (Q_{Ln}^L) determined upon variable wavelength excitation

Complex [(a)]	τ_4 (ms) 300 K	τ_4 (ms) 11 K	λ_{exc} nm	Q_{Ln}^L Solid	Q_{Ln}^L Solution[(c)]
I	0.814 ± 0.002	0.882 ± 0.002	272	0.71 ± 0.07	(not measured)
			320	0.90 ± 0.09	
			365 [(b)]	0.45 ± 0.05	
II	0.969 ± 0.005	1.112 ± 0.001	272	0.88 ± 0.09	0.50 ± 0.05
			320	0.92 ± 0.09	0.55 ± 0.06
			365 [(b)]	0.62 ± 0.06	0.41 ± 0.04

[(a)] τ_T (ligand) = *ca.* 0.9 ms for λ_{em}= 480 nm and λ_{exc}= 385 nm at 300 K. (b) Measurements at 365 nm are mainly due to the $^7F_6 \rightarrow {}^5G_5$ transition of the Tb^{3+} ion (Figure S12a). (c) Solution in dichloromethane 5 mg mL^{-1} (7.6 mmol L^{-1}).

Because of its better emitting performance in the solid-state, complex **II** was also employed in measurements of photoluminescence lifetime and absolute quantum yields in dichloromethane solution (dcm, 7.6 mmol L^{-1}). The τ_4 value in dcm was equal to 1.031 ms, and Q_{Ln}^L was added to Table 3. Despite the higher probability of non-radiating processes in solution, the results provided by **II** are still excellent, confirming the robustness of the structural and energy matchings between the Ln^{3+} ion and the organic

ligand in the terbium system. The distinctive quantum yield values measured for different excitation wavelengths are discussed below in the *Estimation of IET Rates and Absolute Emission Quantum Yields, and Dependence on Excitation Wavelengths* section.

The Eu^{3+}-based complexes **III** and **IV** did not present photoemission at room temperature but only at 11 K, Figure S14. Considering the energy-level diagrams for complexes **III** and **IV** (left-hand side of Figure S14), it is probable that the $^5D_{0\text{-}3}$ levels of Eu^{3+} are also populated via ligand singlet states, as it happens with **I** and **II**. However, low-lying charge-transfer (LMCT) states in the visible region, or a photoinduced electron transfer (PeT) event, known to operate in europium(III) compounds, may be responsible for quenching the luminescence of **III** and **IV** at room temperature.[52, 108-110] The crystals of both complexes are indeed intensely colored (bright- to gold-yellow, Figure S15), differently from the observed for the Tb^{3+} (light pink) and Gd^{3+} (colorless) analogs. A very interesting description of a complete quenching of Eu^{3+} luminescence upon deprotonation of a hydroxyquinoline ligand has been made,[111] and this might relate to the phenolate groups in **III** and **IV**. In the quinoline case, the quenching was attributed to an increase in electron density on the *antenna* following deprotonation, facilitating transient oxidation and consequent deactivation of the ligand excited state by a PeT or LMCT process.[111] Considering products **III** and **IV**, a comprehensive investigation of the nature of such efficient deactivation is yet to be carried out, being outside the immediate reach of the present work.

To understand these findings and elucidate the preferential pathways for ligand-to-Tb^{3+} energy transfer, as well as quantify the transfer rates, a new theoretical approach was developed as described in the following subsections.

In Silico Experiments

In this work, to address the problem of estimating photophysical properties such as intensity parameters (Ω_λ), radiative emission coefficients (A_{rad}) and theoretical quantum yield (Q_{Ln}^L) for Tb^{3+} compounds, we started from isostructural complexes of Eu^{3+} and Tb^{3+} so that the Eu^{3+} compound was used as a reference. This approach was necessary because Tb^{3+} luminescence transitions are characterized by strong magnetic dipole contributions; these must be taken away before the values of the intensity parameters (Ω_λ^{exp}) are extracted from absorption spectra through the oscillator strength fitting procedure.

Accordingly, DFT geometry optimization at the B3LYP/MWB52(Eu)/6-311++G(d,p) level of theory was used to obtain a simulated structure for [Eu(bbp**Y**n)Cl] (**Y** = e, p) (complexes **III** and **IV**), which was then compared with the molecular dimensions (bond lengths and angles) determined by single-crystal X-ray

diffraction analysis (Tables S4 and S5). The agreement between the sets of data is very good (Figure S16), as confirmed by the root mean square deviation (r.m.s.d.) of atomic positions calculated for the whole structure, which equals 0.147 Å for complex **III**. This deviation parameter decreases significantly to 0.064 Å when only the first coordination sphere of the Eu^{3+} ion is considered.

The determination of photophysical properties of the luminescent Tb^{3+} complexes **I** and **II** from isostructural **III** and **IV** was based on the following steps: (i) extraction of intensity parameters, particularly Ω_λ^{exp}, from the Eu^{3+} emission spectra, followed by determination of the theoretical counterpart, Ω_λ^{theo}; (ii) from Ω_λ^{theo}, separation of the quantities (α', α_{OP} and g) that describe the chemical environment around the Ln^{3+} ion; (iii) simulation of the Tb^{3+} response to the same environment experienced by Eu^{3+}, and (iv) estimation of Intramolecular Energy Transfer (IET) rates and Q_{Ln}^L using an appropriate system of rate equations. Details of this procedure are presented as Electronic Supplementary Information (*Theoretical calculations*).

Estimation of IET Rates and Absolute Emission Quantum Yields, and Dependence on Excitation Wavelengths

It has been reported, for a range of Eu^{3+}-based compounds[112] and Tb^{3+}/Ce^{3+} in doped layered silicates,[113] that the lifetime of the emitting ^5D_J level depends on the excitation energy provided to the system. To add to those findings, we carried out a detailed study on the intramolecular energy transfer (IET) processes involving the Tb^{3+} complexes **I** and **II**, focusing on their relationship with the excitation wavelengths and their effect on the overall quantum yield Q_{Ln}^L.

Data on Table 3 indicate different IET dynamics for [Tb(bbp**Y**n)Cl] (Y = e, p) excited at (i) 272 nm, (ii) 320 nm, and (iii) 365 nm, both in the solid-state and dichloromethane solution. The observed dependence of the Q_{Ln}^L values of **I** and **II** on these wavelengths results from the principal processes summarized in Figure 4. For the numerical rates, please refer to Tables S13 and S14.

i) Following excitation at 272 nm (36765 cm^{-1}), the energy is transferred mainly from the S_3 to the $^5F_4$, $^5F_5$, and $^5H_4$ states (summed rates of *ca.* 5.09×10^6 s^{-1}; see Table S13). From there, the energy can bounce to the S_2 (320 nm) with a faster rate (1.36×10^7 s^{-1}).

ii) For excitation at 320 nm (31250 cm^{-1}), the forward energy transfer ($S_2\rightarrow{}^5G_6$) is eight times faster than the backward $^5G_6\rightarrow S_1$.

iii) The excitation at 365 nm (27400 cm^{-1}), in turn, has the largest forward/backward ratio of up to 100. However, at this point, the $S_1\rightarrow T_1$ intersystem crossing rate (W_{ISC}) becomes important due to the energy proximity between the S_1 (27100 cm^{-1}) and T_1 (21000 cm^{-1}) states.

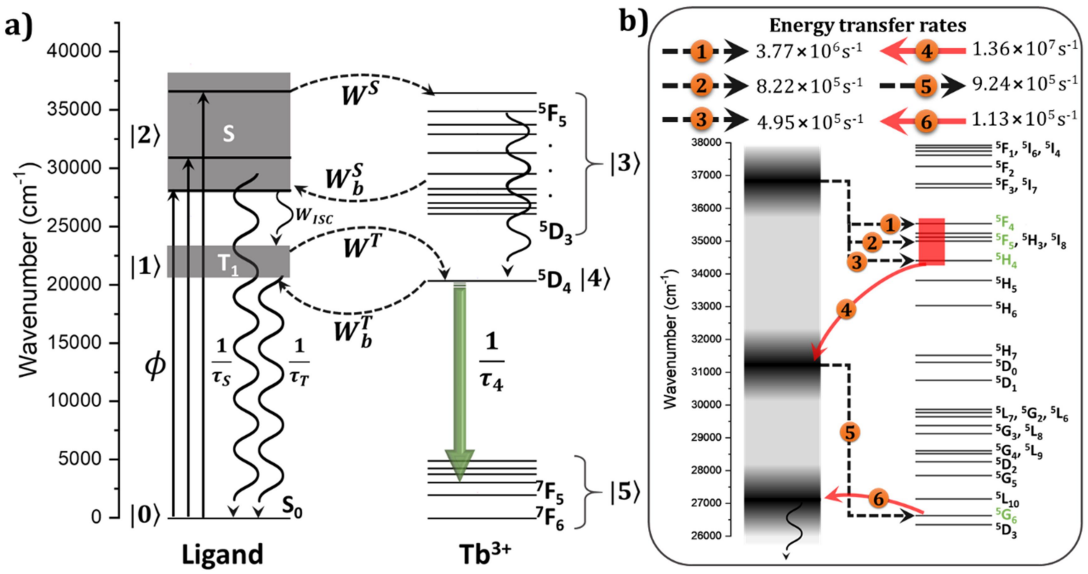

Figure 4. a) Energy level diagram for the [Tb(bbpYn)Cl] (Y = e, p) complexes. τ_s is the singlet decay time, W^T and W^S refer to the energy transfer rates from the T_1 and singlet (S_1, S_2, and S_3) states to the Tb^{3+} energy levels, respectively. Their corresponding backward energy transfer rates are indicated with a subscript ***b***. The decay lifetimes of T_1 (τ_T) and the emitting level $^5D_4$ (τ_4) are given in Table 3. The symbol ϕ refers to the pumping rate. The labels |P⟩ (P = 0, 1, 2, 3, 4, and 5) represent the set of states used for solving the system of rate equations (Electronic Supplementary Information). **b)** Magnified picture illustrating the energy dynamics between the ligand singlets (left) and Tb^{3+} states (right) with emphasis on the excitation wavelengths, as described in detail throughout the text. Broken black arrows denote forward processes, while solid red ones correspond to backward steps. The numbers on the arrows refer to the highest rates listed for each excitation wavelength in Table S13.

All processes described above include the lower energy dynamics when applicable, meaning that the process *i*) includes *ii*) and *iii*); the process *ii*) involves *iii*), and the process *iii*) is considered alone. Consequently, W_{ISC} should be considered for all dynamic processes, as the S_1 state is populated regardless of the excitation wavelength (272, 320, or 365 nm).

Table S13 shows the forward and backward IET rates for 46 pathways related to the 272, 320, and 365 nm excitation wavelengths. The IET rates involving the T_1 state are independent on the excitation wavelength because the population of this state depends mainly on the ISC rate and the backward energy transfer from the $^5G_6$ level (Table S14).

The quantum yield Q_{Ln}^L (Eq. 6) can be estimated by solving an appropriate system of rate equations in the steady-state regime, as detailed in the Electronic Supplementary Information. The final expression presented below indicates how Q_{Ln}^L depends on the lifetimes (τ) and IET rates (W). W_{ISC} and τ_S are the variables gathered in Figure 5, which is discussed as follows.

$$Q_{Ln}^{L} \cong (A_{rad})\frac{N_4}{\phi N_0} = \left(\frac{\tau_4\tau_S}{\tau_4(11K)}\right)\left[\frac{\left[W_{3\to4}W^S + \tau_T W^T\left(W_{ISC}W_b^S + C(W_{ISC}+W^S)\right)\right]}{[W_b^S(1+\tau_S W_{ISC}) + C(1+\tau_S W_{ISC}+\tau_S W^S)][\tau_T W^T + 1 + \tau_4 W_b^T]}\right] \quad (6)$$

In Eq. 6, the emitted photons are given by the product $A_{rad}N_4$, being A_{rad} the spontaneous emission coefficient of the emitting level (|4⟩, $^5D_4$ for Tb^{3+}) with a population of N_4. The absorbed photons are given by the product ϕN_0, being ϕ the pumping rate and N_0 the population in the ligand ground state S_0. The indexes T and S represent the ligand state involved in the quantity, the subscript *b* indicates the backward energy transfer rate (energy from Ln^{3+} to the ligand), and the constant $C = W_{3\to4} + W_{3\to1} = 3.1\times10^5 + 10\times10^5\ s^{-1}$ is the sum of the energy transfers from state |3⟩ (levels above $^5D_4$) to states |4⟩ ($^5D_4$) and |1⟩ (T_1). W_{ISC} is the intersystem crossing rate, which is very sensitive to the energy gap ΔE_{S-T} between the S_1 and T_1 state.[114] The W_{ISC} can vary by orders of magnitude even in molecules with similar structures and ΔE_{S-T}, as studied by El-Sayed in the cases of naphthalene (W_{ISC} = 10^5 s^{-1}) and quinoline (W_{ISC} = 10^8 s^{-1}),[115] depending also on the strength of the spin-orbit interaction.[116]

Figure 5 shows the calculated behavior of Q_{Ln}^{L} *versus* W_{ISC} and τ_S (singlet state lifetime) for each excitation wavelength. The data were statistically treated by weighted least squares and a total of 9800 points (values of Q_{Ln}^{L}) for each surface were used. In all cases, Q_{Ln}^{L} increases when both W_{ISC} and τ_S grow, confirming the importance of both triplet and singlet states in the IET process, as emphasized below.

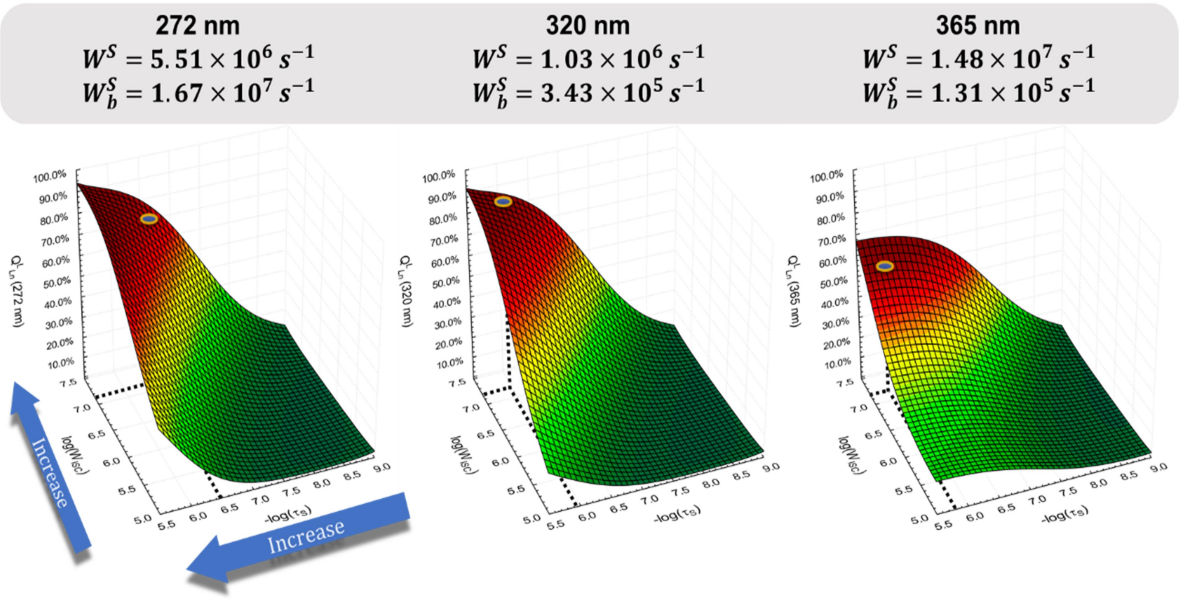

Figure 5. Quantum yields (Q_{Ln}^{L}) as a function of the ISC rates (W_{ISC}) and fluorescence lifetimes (τ_S). Both rates are in log scale, log(W_{ISC}) and -log(τ_S). The highlighted regions indicate the matchings with the experimental data.

Complexes **I** and **II** constitute an interesting case in which both the singlet and triplet states of the ligands are relevant for the photophysical properties of the system. On one hand, the population of the T_1 state grows when W_{ISC} increases; on the other, the population of the S_1 state grows when the τ_S lifetime increases, and both populations contribute to the rise in Q_{Ln}^{L}. Considering that the oscillator strengths (***f***, Figure S8b) follow the trend *f*(272 nm) > *f*(320 nm) > *f*(365 nm), the higher the ***f*** value, the more allowed is the absorption and also the opposite process (the fluorescence). Thus, a shorter singlet lifetime is expected for the excitation at 272 nm. Accordingly, the observation of the 272 and 320 nm surfaces of Figure 5 evidences that the values of $Q_{Ln(320\ nm)}^{L}$ lie close to the maximum of 90% while those of $Q_{Ln(272\ nm)}^{L}$ are located around 80% (see highlighted regions), in agreement with the experimental values in Table 3.

Lastly, both the **bbpen**$^{2-}$ and **bbppn**$^{2-}$ ligands, Figure S10a for [Gd(bbppn)Cl], absorb poorly at 365 nm. In fact, the absorption in this region is mostly attributed to the $^7F_6 \rightarrow {}^5G_5$ transition of the Tb^{3+} ion (as shows Figure S12a). This implies longer values of τ_S (in the order of μs), leading to Q_{Ln}^{L}(365 nm) around 60% and corroborating the calculated (Figure 5) and measured (Table 3) results.

Photostability and Preparation of a Downshifting Layer for a UV-LED Device

Photostability is an important requisite for the development of optoelectronic devices. Recent studies have shown that Ln^{3+} complexes generally suffer photodegradation upon continuous illumination,[117-121] which is attributed to possible molecular interactions in the solid-state or intense vibrations of the complex after absorbing light. The first phenomenon leads to dissipation of the energy absorbed by the ligand,[118] while vibrations may result in fast molecular decomposition.[117] For instance, J. Kai *et al.* showed that $[Tb(acac)_3(H_2O)_3]$ loses 53% of its initial emission intensity after illumination at 340 nm during 6 hours; this loss was reduced to 8% by dispersing in a poly(methylmethacrylate) (PMMA) matrix.[121] Recently, Lapaev *et al.* reported a Tb^{3+} β-diketonate complex denoted as $[Tb(CPDK_{3\text{-}7})_3(phen)]$, where $CPDK_{3\text{-}7}$ is 1-(4-(4-propylcyclohexyl)phenyl)decane-1,3-dione and phen=1,10-phenanthroline, which was melted at 405 K and vitrified between two quartz plates to reduce the exposition to oxygen.[122] Upon illumination at 337 nm, the vitrified film showed no degradation up to 4.5 hours; no information was given on longer exposition times. In another approach, $[Eu(tta)_3(ephen)]$, ephen = 5,6-epoxy-5,6-dihydro-[1,10]phenanthroline, suffered a reduction of 70% on its emission intensity in the first two hours of illumination at 365 nm; this photo-bleaching process was reduced to ca. 30% (10 hours of exposition) by incorporation of the complex in an organic-inorganic tri-ureasil matrix.[123]

In the present work, although both products **I** and **II** are soluble in dichloromethane, only complex **II** was investigated as a potential downshifting layer due to its superior luminescence properties. As shown

in Table 3, a significant Q_{Ln}^{L} value of 0.55 ± 0.06 was measured for a 7.6 mmol L^{-1} solution of **II** in dcm, and this solution produced homogeneous thin films by drop-casting on a substrate at room temperature. Notably, the composition of **II**, and therefore the chemical environment of the Tb^{3+} ion, was preserved after solubilization and preparation of the thin film, as indicated by the optical and XRD data presented in Figures S17 and S18. These features, together with the photo-stability of the complex upon UV illumination in air without dispersion into a hybrid host (maximum 10% loss of emission intensity after 10 h of continuous excitation at 325 nm, Figure S19c), allowed the direct application of the film as a green-emitting layer onto a UV-LED chip (365 nm). Figure 6 shows the results concerning the [Tb(bbppn)Cl]-coated UV-LED. The green emission is characterized by (x,y) CIE color coordinates in the yellowish-green spectral range of (0.33,0.58). Since we are quantifying the emission color of the phosphor, the emission spectra are governed by the typical intra-4f^8 $^5D_4 \rightarrow {}^7F_{6-3}$ transitions. The higher relative intensity and low FWHM (full width at half-maximum, <10 nm) of the $^5D_4 \rightarrow {}^7F_6$ transition in the green spectral range (peaking around 545 nm) is responsible for the color purity, when compared with other green-emitting phosphors based on Eu^{2+} ($^4F_6$ $^5D_1 \rightarrow {}^4F_7$) or Ce3+ ($^4F_6$ $^5D_1 \rightarrow {}^4F_1$).[124] The emission was further quantified by the photometric luminous flux (0.587 lm) and luminous efficacy of radiation (η=6.1 lm/W) when submitted to a current of 30 mA. Comparatively (Table S15), this value of η is 7.6 times higher than the response achieved with $[Tb(3Cl\text{-}acac)_3(H_2O)_2]$ at the same excitation wavelength,[125] and is similar to the luminance efficiency (7.12 lm/W) of the commercial Ce^{3+}/Tb^{3+}-co-doped $Ca_3Sc_2Si_3O_{12}$ coating layer on InGaN-blue emitting LEDs (460 nm).[126]

To the best of our knowledge, the highest η values (Table S15) reported for molecular Tb^{3+} complexes in LED prototypes refer to $[Tb(p\text{-}BBA)_3(UA)]$[127] and $[Tb(p\text{-}BBA)_3(MAA)]$[128] after excitation at 365 nm, with p-BBA = 4-benzoylbenzoic acid, UA = undecylenic acid and MAA = methacrylic acid. These compounds presented η = 17.3 and 18.6 lm/W under 350 mA (respectively) after mixing with silicone and curing at 150 °C;[127-128] however, none of them was characterized by single-crystal X-ray diffraction analysis or mass spectrometry or had quantum yields determined in the solid state. If, on the other hand, the mixed-metal $Tb_3Al_5O_{12}:Ce^{3+}$ oxide (TAG:Ce) coating on InGaN (for the fabrication of white LEDs) gives 34.1 lm/W at 20 mA,[129] its preparation requires firing high purity Ln oxides at 1500 °C in a reducing atmosphere.[130] Such a solid-state route is dramatically different from the mild synthetic conditions employed in this work for preparing complexes **I** and **II**.

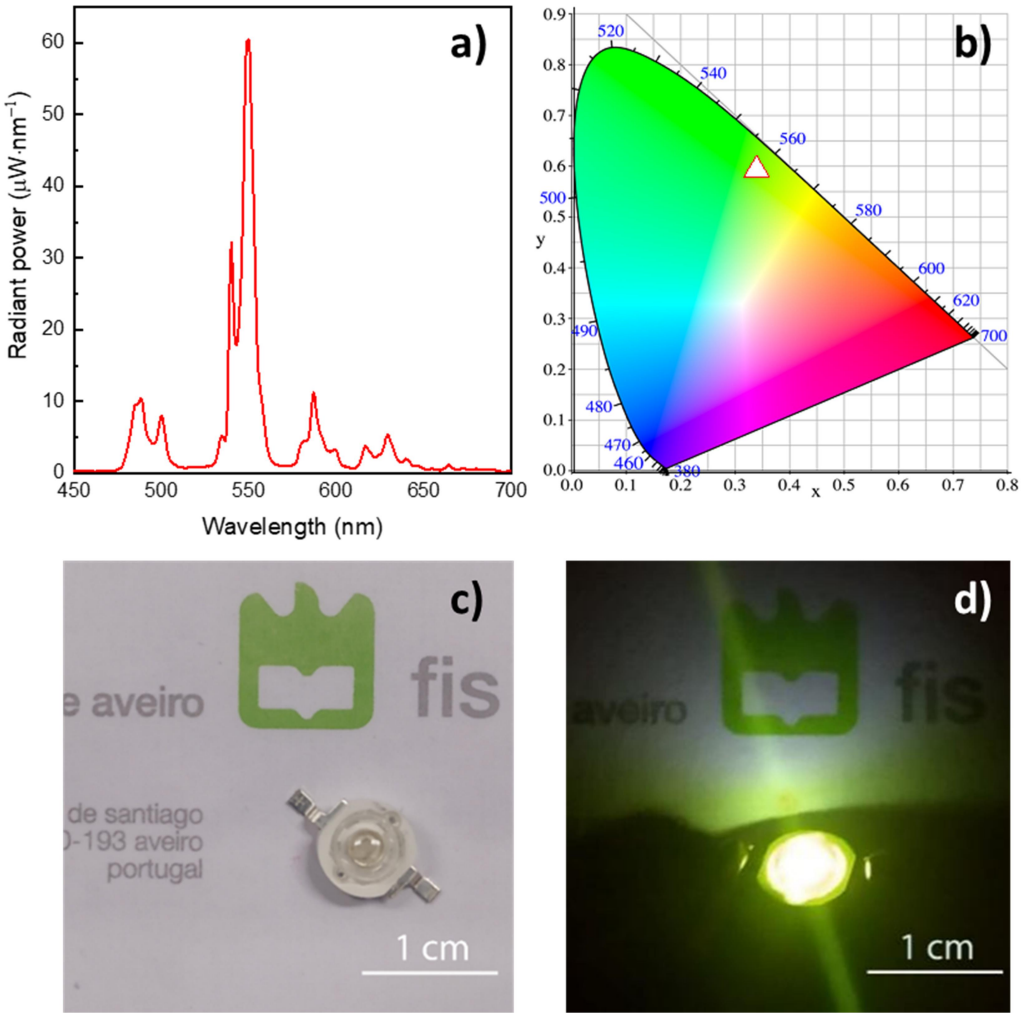

Figure 6. a) Room-temperature emission spectra of the LED phosphor produced with complex **II**; b) color coordinates in CIE 1931 chromaticity map; c) and d) commercial 365 LED chip coated with a film of complex **II**, with 30 mA of driving current upon 3.2 V.

The emission stability of the LED prototypes made with complex **II** was monitored for 11 hours. The intensities remained constant with no color shift, Figure S19a, confirming that **II** may be used as a UV-downshifting phosphor for green-emitting LEDs. Moreover, the intensity of the fabricated LED (operated with 3.2 V) displays less than 10% degradation after more than 10 hours of continuous working, Figure S19b. This photo-bleaching resistance of pure **II** in a thin film, even without incorporation in any organic or inorganic matrix and without thermal treatment, is much higher than that reported for other Tb^{3+} and Eu^{3+} complexes with ligands such as β-diketonates.[121, 123, 125] Considering that many possible structural changes can be made to these ethylenediamine-based ligands before preparing the derived Ln^{3+} compounds, such chemical versatility and robustness are advantages of these chemical species in potential optical applications such as integration in UV-LEDs or photovoltaics.

CONCLUSIONS

Despite their wide use in several fields of coordination and analytical chemistry due to easy and versatile synthesis, ethylenediamine-based polydentate ligands have not been widely explored in photoluminescence studies. Here we show that the simple combination of phenolate and pyridine rings as substituents on the ethylenediamine backbone produces robust and efficient *antennas* for Tb^{3+} ions. Emission quantum yields as high as 92% in the solid-state, convenient excited-state lifetimes of *ca.* 1.0 ms, and remarkable stability (in air, under irradiation, and in thin films) are positive features of the products here described. Synthetic tailoring of these ligands and the coordination sphere, together with possible insertion in organic/inorganic polymeric matrices, are wide-open possibilities for this promising system.

A comprehensive structural, chemical, and spectroscopic characterization of six lanthanide complexes of en-based ligands was described in the present study. The two Tb^{3+} complexes **I** and **II** display slow magnetic relaxation with an applied static field, in striking contrast with the behavior of the Dy^{3+} analogs, suggesting their non-Kramers nature to be a ruling factor in determining the magnetization dynamics. Comparison of the magnetic data and optical emission spectra at low temperature suggests a Raman/direct mechanism to be active for both Tb^{3+} compounds.

Highly efficient energy transfer from the *antenna* ligands has been revealed for both products **I** and **II**. Such efficiency, combined with robustness, allowed the fabrication of bright green-emitting LED prototypes. In this work, we also introduced a new theoretical model, based on the intramolecular energy transfer dynamics, to rationalize the dependence of emission quantum yields on the excitation wavelengths. The results evidenced that the Tb(bbp**Y**n)Cl complexes (Y = e, p) are good molecular examples in which both triplet and singlet excited states provide energy to the Tb^{3+} ion and lead to high values of Q_{Ln}^{L}.

The relevance of the regular pentagonal-bipyramidal geometry around Tb^{3+} for the matching of energy states or inhibition of excited-state deactivation processes is worth further investigation for the establishment of new optical-structural correlations. Based on the findings here described, and in line with recent reports about the enhancement of magnetic and optical properties in seven-coordinate environments,[28, 52] the combination of PBP geometry and suitable en-based ligands may provide substantially improved magnetic, photo- and electro-luminescent Ln^{3+}-based materials.

ACKNOWLEDGEMENTS

This study was financially supported by Fundação Araucária (grants 20171010 and 283/2014, protocol 37509), Conselho Nacional de Desenvolvimento Científico e Tecnológico (CNPq, grant 308426/2016-9), Coordenação de Aperfeiçoamento de Pessoal de Nível Superior (CAPES, Finance Code 001), Serrapilheira Institute (grant Serra-1709-17054), and Fundação de Amparo à Pesquisa do Estado do Rio de Janeiro (FAPERJ, Grants E-26/202.912/2019, SEI-260003/001167/2020 and E-26/010.000978/2019). The work was also developed within the scope of the project CICECO-Aveiro Institute of Materials, UIDB/50011/2020 & UIDP/50011/2020, financed by national funds through the FCT/MEC and, when appropriate, co-financed by FEDER under the PT2020 Partnership Agreement. L.E.N.A, G.A.B., J.L.R., F.S.S., S.O.K.G., D.L.H., G.P., A.G.M., and J.F.S. thank the Brazilian agencies CNPq, CAPES, FAPERJ, and Fundação Araucária for fellowships. A.N.C.N.'s work was financially supported by the project SusPhotoSolutions, CENTRO-01-0145-FEDER-000005, funded by FEDER, through POCI, and by national funds through FCT/MCTES. G.P. gratefully acknowledges Prof. Luis Ghivelder (Institute of Physics, Federal University of Rio de Janeiro) for providing access to the magnetic characterization equipment.

ASSOCIATED CONTENT

Supporting information

The Supporting Information is available free of charge at https://pubs.acs.org/

Tables of crystallographic, magnetic susceptibility, optical, and theoretical data (Tables S1-S16); plots of spectroscopic (Figures S1, S8-S17, S19), structural (Figures S2-S4, S18) and magnetic (Figures S5-S7) measurement results; details on theoretical calculations (Figures S20-22; PDF).

Accession Codes

CCDC 1905766, and 1987799-1987803 contain the supplementary crystallographic data for this paper. These data can be obtained free of charge via www.ccdc.cam.ac.uk/data_request/cif, or by emailing data_request@ccdc.cam.ac.uk, or by contacting The Cambridge Crystallographic Data Centre, 12 Union Road, Cambridge CB2 1EZ, UK; fax: +44 1223 336033.

AUTHOR INFORMATION

Corresponding authors

Luís D. Carlos – *Phantom-g, CICECO – Aveiro Institute of Materials, Department of Physics, University of Aveiro, 3810-193 – Aveiro, Portugal; orcid.org/0000-0003-4747-6535*; E-mail: lcarlos@ua.pt.

Andreia G. Macedo - *Department of Physics, Federal University of Technology, 80230-901 – Curitiba-PR, Brazil and Phantom-g, CICECO – Aveiro Institute of Materials, Department of Physics and*

University of Aveiro, 3810-193 – Aveiro, Portugal; orcid.org/0000-0002-3114-9954; Email: agmacedo@utfpr.edu.br

Jaísa F. Soares - *Department of Chemistry, Federal University of Paraná, 81530-900 – Curitiba-PR, Brazil; orcid.org/0000-0002-2775-131X;* Email: jaisa@quimica.ufpr.br

Authors

Lucas E. do N. Aquino - *Department of Chemistry, Federal University of Paraná, 81530-900 – Curitiba-PR, Brazil;*

Guilherme A. Barbosa - *Department of Chemistry, Federal University of Paraná, 81530-900 – Curitiba-PR, Brazil;*

Jaqueline de L. Ramos - *Department of Chemistry, Federal University of Paraná, 81530-900 – Curitiba-PR, Brazil;*

Siddhartha O. K. Giese - *Department of Chemistry, Federal University of Paraná, 81530-900 – Curitiba-PR, Brazil;*

Francielli S. Santana - *Department of Chemistry, Federal University of Paraná, 81530-900 – Curitiba-PR, Brazil; orcid.org/0000-0003-4570-3044;*

David L. Hughes - *School of Chemistry, Federal University of East Anglia, Norwich NR4 7TJ, UK; orcid.org/0000-0003-0621-204X;*

Giovana G. Nunes - *Department of Chemistry, Federal University of Paraná, 81530-900 – Curitiba-PR, Brazil; orcid.org/0000-0001-7052-2523;*

Lianshe Fu - *Phantom-g, Department of Physics, CICECO – Aveiro Institute of Materials, University of Aveiro, 3810-193 – Aveiro, Portugal; orcid.org/0000-0002-9887-371X;*

Ming Fang - *Phantom-g, Department of Physics, CICECO – Aveiro Institute of Materials, University of Aveiro, 3810-193 – Aveiro, Portugal; orcid.org/0000-0002-7406-0466;*

Giordano Poneti - *Institute of Chemistry, Federal University of Rio de Janeiro, 21941-909 – Rio de Janeiro-RJ, Brazil; orcid.org/0000-0002-1712-4611;*

Albano N. Carneiro Neto - *Phantom-g, Department of Physics, CICECO – Aveiro Institute of Materials, University of Aveiro, 3810-193 – Aveiro, Portugal; orcid.org/0000-0003-2432-0992;*

Renaldo T. Moura Jr. - *Department of Chemistry and Physics, Federal University of Paraíba, 58397-000 – Areia-PB, Brazil; orcid.org/0000-0002-8151-1640;*

Rute A. S. Ferreira - *Phantom-g, Department of Physics, CICECO – Aveiro Institute of Materials, University of Aveiro, 3810-193 – Aveiro, Portugal; orcid.org/0000-0003-1085-7836.*

Complete contact information is available at: https://pubs.acs.org/

Notes

The authors declare no competing financial interest.

REFERENCES

(1) Bunzli, J. C. G., Lanthanide Photonics: Shaping the Nanoworld. *Trends Chem.* **2019,** *1* (8), 751-762.

(2) Hasegawa, Y.; Kitagawa, Y.; Nakanishi, T., Effective Photosensitized, Electrosensitized, and Mechanosensitized Luminescence of Lanthanide Complexes. *NPG Asia Mater.* **2018,** *10* (4), 52-70.

(3) McAdams, S. G.; Ariciu, A. M.; Kostopoulos, A. K.; Walsh, J. P. S.; Tuna, F., Molecular Single-Ion Magnets Based on Lanthanides and Actinides: Design Considerations and New Advances in the Context of Quantum Technologies. *Coord. Chem. Rev.* **2017,** *346*, 216-239.

(4) Bünzli, J. C. G., Lanthanides. In *Kirk-Othmer Encyclopedia of Chemical Technology*, Ley, C., Ed. Wiley-VCH: 2013; pp 1-43.

(5) Fernandes, M.; Freitas, V.; Pereira, S.; Leones, R.; Silva, M. M.; Carlos, L. D.; Fortunato, E.; A. S. Ferreira, R.; Rego, R.; De Zea Bermudez, V., Luminescent Electrochromic Devices for Smart Windows of Energy-Efficient Buildings. *Energies* **2018,** *11* (12), 3513.

(6) Choi, S. H.; Duzik, A. J.; Kim, H. J.; Park, Y.; Kim, J.; Ko, H. U.; Kim, H. C.; Yun, S.; Kyung, K. U., Perspective and Potential of Smart Optical Materials. *Smart Mater. Struct.* **2017,** *26* (9).

(7) Brites, C. D. S.; Balabhadra, S.; Carlos, L. D., Lanthanide-Based Thermometers: At the Cutting-Edge of Luminescence Thermometry. *Adv. Opt. Mater.* **2019,** *7* (5).

(8) Allison, S. W., A Brief History of Phosphor Thermometry. *Meas. Sci. Technol.* **2019,** *30* (7).

(9) Brites, C. D. S.; Millán, A.; Carlos, L. D., Chapter 281 - Lanthanides in Luminescent Thermometry. In *Handbook on the Physics and Chemistry of Rare Earths*, Jean-Claude, B.; Vitalij K, P., Eds. Elsevier: 2016; Vol. 49, pp 339-427.

(10) Liu, J. Q.; Luo, Z. D.; Pan, Y.; Singh, A. K.; Trivedi, M.; Kumar, A., Recent Developments in Luminescent Coordination Polymers: Designing Strategies, Sensing Application and Theoretical Evidences. *Coord. Chem. Rev.* **2020,** *406*.

(11) Aulsebrook, M. L.; Graham, B.; Grace, M. R.; Tuck, K. L., Lanthanide Complexes for Luminescence-Based Sensing of Low Molecular Weight Analytes. *Coord. Chem. Rev.* **2018,** *375*, 191-220.

(12) Mahata, P.; Mondal, S. K.; Singha, D. K.; Majee, P., Luminescent Rare-Earth-Based Mofs as Optical Sensors. *Dalton Trans.* **2017,** *46* (2), 301-328.

(13) McGhee, C. E.; Loh, K. Y.; Lu, Y., Dnazyme Sensors for Detection of Metal Ions in the Environment and Imaging Them in Living Cells. *Curr. Opin. Biotechnol.* **2017,** *45*, 191-201.

(14) Himmelstoss, S. F.; Hirsch, T., A Critical Comparison of Lanthanide Based Upconversion Nanoparticles to Fluorescent Proteins, Semiconductor Quantum Dots, and Carbon Dots for Use in Optical Sensing and Imaging. *Methods Appl. Fluor.* **2019,** *7* (2).

(15) Kumamoto, Y.; Taguchi, A.; Kawata, S., Deep-Ultraviolet Biomolecular Imaging and Analysis. *Adv. Opt. Mater.* **2019,** *7* (5).

(16) Hewitt, S. H.; Butler, S. J., Application of Lanthanide Luminescence in Probing Enzyme Activity. *Chem. Commun.* **2018,** *54* (50), 6635-6647.

(17) Sedgwick, A. C.; Brewster, J. T.; Harvey, P.; Iovan, D. A.; Smith, G.; He, X. P.; Tian, H.; Sessler, J. L.; James, T. D., Metal-Based Imaging Agents: Progress Towards Interrogating Neurodegenerative Disease. *Chem. Soc. Rev.* **2020,** *49* (10), 2886-2915.

(18) Clough, T. J.; Jiang, L. J.; Wong, K. L.; Long, N. J., Ligand Design Strategies to Increase Stability of Gadolinium-Based Magnetic Resonance Imaging Contrast Agents. *Nat. Commun.* **2019,** *10*, article 1420.

(19) Gotzke, L.; Schaper, G.; Marz, J.; Kaden, P.; Huittinen, N.; Stumpf, T.; Kammerlander, K. K. K.; Brunner, E.; Hahn, P.; Mehnert, A.; Kersting, B.; Henle, T.; Lindoy, L. F.; Zanoni, G.; Weigand, J. J., Coordination Chemistry of F-Block Metal Ions with Ligands Bearing Bio-Relevant Functional Groups. *Coord. Chem. Rev.* **2019,** *386*, 267-309.

(20) Bünzli, J.-C. G., Lanthanide Light for Biology and Medical Diagnosis. *J. Lumin.* **2016,** *170*, 866-878.

(21) Ning, Y. Y.; Cheng, S. M.; Wang, J. X.; Liu, Y. W.; Feng, W.; Li, F. Y.; Zhang, J. L., Fluorescence Lifetime Imaging of Upper Gastrointestinal Ph in Vivo with a Lanthanide Based near-Infrared Tau Probe. *Chem. Sci.* **2019,** *10* (15), 4227-4235.
(22) Ning, Y.; Zhu, M.; Zhang, J.-L., Near-Infrared (Nir) Lanthanide Molecular Probes for Bioimaging and Biosensing. *Coord. Chem. Rev.* **2019,** *399*, 213028.
(23) Gillam, T. A.; Sweetman, M. J.; Bader, C. A.; Morrison, J. L.; Hayball, J. D.; Brooks, D. A.; Plush, S. E., Bright Lights Down Under: Metal Ion Complexes Turning the Spotlight on Metabolic Processes at the Cellular Level. *Coord. Chem. Rev.* **2018,** *375*, 234-255.
(24) Dushyantha, N.; Batapola, N.; Ilankoon, I. M. S. K.; Rohitha, S.; Premasiri, R.; Abeysinghe, B.; Ratnayake, N.; Dissanayake, K., The Story of Rare Earth Elements (Rees): Occurrences, Global Distribution, Genesis, Geology, Mineralogy and Global Production. *Ore Geol. Rev.* **2020,** *122*, 103521.
(25) Binnemans, K.; Jones, P. T.; Müller, T.; Yurramendi, L., Rare Earths and the Balance Problem: How to Deal with Changing Markets? *J. Sustainable Metall.* **2018,** *4* (1), 126-146.
(26) Bünzli, J.-C. G., Rising Stars in Science and Technology: Luminescent Lanthanide Materials. *Eur. J. Inorg. Chem.* **2017,** *2017* (44), 5058-5063.
(27) Bünzli, J.-C. G., On the Design of Highly Luminescent Lanthanide Complexes. *Coord. Chem. Rev.* **2015,** *293-294*, 19-47.
(28) Kalita, P.; Acharya, J.; Chandrasekhar, V., Mononuclear Pentagonal Bipyramidal Ln(Iii) Complexes: Syntheses and Magnetic Properties. *J. Magn. Magn. Mater.* **2020,** *498*, 166098.
(29) Guo, F.-S.; Day, B. M.; Chen, Y.-C.; Tong, M.-L.; Mansikkamäki, A.; Layfield, R. A., Magnetic Hysteresis up to 80 Kelvin in a Dysprosium Metallocene Single-Molecule Magnet. *Science* **2018,** *362* (6421), 1400-1403.
(30) Goodwin, C. A. P.; Ortu, F.; Reta, D.; Chilton, N. F.; Mills, D. P., Molecular Magnetic Hysteresis at 60 Kelvin in Dysprosocenium. *Nature* **2017,** *548* (7668), 439-442.
(31) Jia, J.-H.; Li, Q.-W.; Chen, Y.-C.; Liu, J.-L.; Tong, M.-L., Luminescent Single-Molecule Magnets Based on Lanthanides: Design Strategies, Recent Advances and Magneto-Luminescent Studies. *Coord. Chem. Rev.* **2019,** *378*, 365-381.
(32) Long, J.; Guari, Y.; Ferreira, R. A. S.; Carlos, L. D.; Larionova, J., Recent Advances in Luminescent Lanthanide Based Single-Molecule Magnets. *Coord. Chem. Rev.* **2018,** *363*, 57-70.
(33) Kovacs, D.; Lu, X.; Mészáros, L. S.; Ott, M.; Andres, J.; Borbas, K. E., Photophysics of Coumarin and Carbostyril-Sensitized Luminescent Lanthanide Complexes: Implications for Complex Design in Multiplex Detection. *J. Am. Chem. Soc.* **2017,** *139* (16), 5756-5767.
(34) Junker, A. K. R.; Sørensen, T. J., Shining Light on the Excited State Energy Cascade in Kinetically Inert Ln(Iii) Complexes of a Coumarin-Appended Do3a Ligand. *Dalton Trans.* **2019,** *48* (3), 964-970.
(35) Junker, A. K. R.; Hill, L. R.; Thompson, A. L.; Faulkner, S.; Sørensen, T. J., Shining Light on the Antenna Chromophore in Lanthanide Based Dyes. *Dalton Trans.* **2018,** *47* (14), 4794-4803.
(36) Kasprzycka, E.; Trush, V. A.; Amirkhanov, V. M.; Jerzykiewicz, L.; Malta, O. L.; Legendziewicz, J.; Gawryszewska, P., Contribution of Energy Transfer from the Singlet State to the Sensitization of Eu3+ and Tb3+ Luminescence by Sulfonylamidophosphates. *Chem. Eur. J.* **2017,** *23* (6), 1318-1330.
(37) Andres, J.; Chauvin, A.-S., Energy Transfer in Coumarin-Sensitised Lanthanide Luminescence: Investigation of the Nature of the Sensitiser and Its Distance to the Lanthanide Ion. *PCCP* **2013,** *15* (38), 15981-15994.
(38) Plyusnin, V. F.; Kupryakov, A. S.; Grivin, V. P.; Shelton, A. H.; Sazanovich, I. V.; Meijer, A. J. H. M.; Weinstein, J. A.; Ward, M. D., Photophysics of 1,8-Naphthalimide/Ln(Iii) Dyads (Ln = Eu, Gd): Naphthalimide → Eu(Iii) Energy-Transfer from Both Singlet and Triplet States. *Photochem. Photobiol. Sci.* **2013,** *12* (9), 1666-1679.
(39) Baek, N. S.; Kim, Y. H.; Roh, S.-G.; Kwak, B. K.; Kim, H. K., The First Inert and Photostable Encapsulated Lanthanide(Iii) Complexes Based on Dendritic 9,10-Diphenylanthracene Ligands:

Synthesis, Strong near-Infrared Emission Enhancement, and Photophysical Studies. *Adv. Funct. Mater.* **2006,** *16* (14), 1873-1882.

(40) Katkova, M. A.; Borisov, A. V.; Fukin, G. K.; Baranov, E. V.; Averyushkin, A. S.; Vitukhnovsky, A. G.; Bochkarev, M. N., Synthesis and Luminescent Properties of Lanthanide Homoleptic Mercaptothi(Ox)Azolate Complexes: Molecular Structure of Ln(Mbt)3 (Ln=Eu, Er). *Inorg. Chim. Acta* **2006,** *359* (13), 4289-4296.

(41) Yang, C.; Fu, L.-M.; Wang, Y.; Zhang, J.-P.; Wong, W.-T.; Ai, X.-C.; Qiao, Y.-F.; Zou, B.-S.; Gui, L.-L., A Highly Luminescent Europium Complex Showing Visible-Light-Sensitized Red Emission: Direct Observation of the Singlet Pathway. *Angew. Chem. Int. Ed.* **2004,** *43* (38), 5010-5013.

(42) Rodríguez-Cortiñas, R.; Avecilla, F.; Platas-Iglesias, C.; Imbert, D.; Bünzli, J.-C. G.; de Blas, A.; Rodríguez-Blas, T., Structural and Photophysical Properties of Heterobimetallic 4f-Zn Iminophenolate Cryptates. *Inorg. Chem.* **2002,** *41* (21), 5336-5349.

(43) Howell, R. C.; Spence, K. V. N.; Kahwa, I. A.; White, A. J. P.; Williams, D. J., The Preparation and Crystal and Molecular Structures of New Luminescent Schiff-Base Complexes Featuring Coupled Lanthanide(Iii) Cations. *J. Chem. Soc., Dalton Trans.* **1996,** (6), 961-968.

(44) Guerriero, P.; Vigato, P. A.; Bünzli, J.-C. G.; Moret, E., Macrocyclic Complexes with Lanthanoid Salts Part 38. Synthesis and Luminescence Study of Homo- and Hetero-Binuclear Complexes of Lanthanides with a New Cyclic Compartmental Schiff Base. *J. Chem. Soc., Dalton Trans.* **1990,** (2), 647-655.

(45) Bünzli, J.-C. G., Lanthanide Luminescence for Biomedical Analyses and Imaging. *Chem. Rev.* **2010,** *110* (5), 2729-2755.

(46) Utochnikova, V. V.; Kalyakina, A. S.; Solodukhin, N. N.; Aslandukov, A. N., On the Structural Features of Substituted Lanthanide Benzoates. *Eur. J. Inorg. Chem.* **2019,** *2019* (18), 2320-2332.

(47) Ogata, S.; Goto, N.; Sakurai, S.; Ishii, A.; Hatanaka, M.; Yoshihara, K.; Tanabe, R.; Kayano, K.; Magaribuchi, R.; Goto, K.; Hasegawa, M., Alkyl Chain Elongation and Acyl Group Effects in a Series of Eu/Tb Complexes with Hexadentate Π-Electronic Skeletons and Their Enhanced Luminescence in Solutions. *Dalton Trans.* **2018,** *47* (21), 7135-7143.

(48) Hatanaka, M.; Osawa, A.; Wakabayashi, T.; Morokuma, K.; Hasegawa, M., Computational Study on the Luminescence Quantum Yields of Terbium Complexes with 2,2′-Bipyridine Derivative Ligands. *PCCP* **2018,** *20* (5), 3328-3333.

(49) Zou, X.; Yan, P.; Zhang, J.; Zhang, F.; Hou, G.; Li, G., Nir Luminescence and Catalysis of Multifarious Salen Type Ytterbium Complexes Modulated by Anions. *Dalton Trans.* **2013,** *42* (36), 13190-13199.

(50) Gregório, T.; Leão, J. d. M.; Barbosa, G. A.; Ramos, J. d. L.; Om Kumar Giese, S.; Briganti, M.; Rodrigues, P. C.; de Sá, E. L.; Viana, E. R.; Hughes, D. L.; Carlos, L. D.; Ferreira, R. A. S.; Macedo, A. G.; Nunes, G. G.; Soares, J. F., Promoting a Significant Increase in the Photoluminescence Quantum Yield of Terbium(Iii) Complexes by Ligand Modification. *Inorg. Chem.* **2019,** *58* (18), 12099-12111.

(51) Pan, M.; Zheng, X.-L.; Liu, Y.; Liu, W.-S.; Su, C.-Y., Structural and Photoluminescent Studies of Lanthanide Complexes with Tripodal Trirntb (N-Substituted Tris(Benzimidazol-2-Ylmethyl)Amine): Ligand Substituent, Anionic and Secondary Ligand Effects. *Dalton Trans.* **2009,** (12), 2157-2169.

(52) Ferreira da Rosa, P. P.; Kitagawa, Y.; Hasegawa, Y., Luminescent Lanthanide Complex with Seven-Coordination Geometry. *Coord. Chem. Rev.* **2020,** *406*, 213153.

(53) Liu, J.; Chen, Y.-C.; Liu, J.-L.; Vieru, V.; Ungur, L.; Jia, J.-H.; Chibotaru, L. F.; Lan, Y.; Wernsdorfer, W.; Gao, S.; Chen, X.-M.; Tong, M.-L., A Stable Pentagonal Bipyramidal Dy(Iii) Single-Ion Magnet with a Record Magnetization Reversal Barrier over 1000 K. *J. Am. Chem. Soc.* **2016,** *138* (16), 5441-5450.

(54) Jiang, Z.; Sun, L.; Yang, Q.; Yin, B.; Ke, H.; Han, J.; Wei, Q.; Xie, G.; Chen, S., Excess Axial Electrostatic Repulsion as a Criterion for Pentagonal Bipyramidal Dyiii Single-Ion Magnets with High Ueff and Tb. *J. Mater. Chem. C* **2018,** *6* (15), 4273-4280.

(55) Perrin, D. D.; Armarego, W. L., *Purification of Laboratory Chemicals*. 3rd ed.; Butterworth-Heinemann: Oxford, 1997.

(56) Yamada, Y.; Takenouchi, S.-I.; Miyoshi, Y.; Okamoto, K.-I., Syntheses, Crystal Structures, and Some Properties of Heavier Lanthanide(Iii) Complexes with Optically Active N,N ′-Bis(2-Hydroxybenzyl)-N,N ′-Bis(2-Pyridylmethyl)-R-1,2-Propanediamine. *J. Coord. Chem.* **2010,** *63* (6), 996-1012.
(57) Neves, A.; Erthal, S. M. D.; Vencato, I.; Ceccato, A. S.; Mascarenhas, Y. P.; Nascimento, O. R.; Horner, M.; Batista, A. A., Synthesis, Crystal Structure, Electrochemical, and Spectroelectrochemical Properties of the New Manganese(Iii) Complex [Mniii(Bbpen)][Pf6] [H2bbpen = N,N'-Bis(2-Hydroxybenzyl)-N,N'-Bis(2-Methylpyridyl)Ethylenediamine]. *Inorg. Chem.* **1992,** *31* (23), 4749-4755.
(58) Yamada, Y.; Koori, D.; Mori, K.; Oshikawa, Y., Syntheses, Crystal Structures, and Properties of Optically Active Lu(Iii) and Yb(Iii) Complexes of N,N′-Bis(2-Hydroxybenzyl)-N,N′-Bis(2-Pyridylmethyl)-R-1,2-Propanediamine with Chloride or Thiocyanate. *J. Coord. Chem.* **2016,** *69* (24), 3735-3744.
(59) Bruker *Apex3, Saint and Sadabs Software*, Bruker AXS Inc.: Madison, Wisconsin, USA, 2016.
(60) Sheldrick, G., Shelxt - Integrated Space-Group and Crystal-Structure Determination. *Acta Crystallogr. Sect. A* **2015,** *71* (1), 3-8.
(61) Sheldrick, G. M., Crystal Structure Refinement with Shelxl. *Acta Crystallogr. Sec. C: Struct. Chem.* **2015,** *71*, 3-8.
(62) Wilson, A. J. C., *International Tables for X-Ray Crystallography*. Kluwer Academic Publishers: Dordrecht 1992; Vol. C, pp. 500, 219 and 193.
(63) Farrugia, L. J., Wingx and Ortep for Windows: An Update. *J. Appl. Crystallogr.* **2012,** *45*, 849-854.
(64) Farrugia, L. J., Wingx Suite for Small-Molecule Single-Crystal Crystallography. *J. Appl. Crystallogr.* **1999,** *32* (4), 837-838.
(65) Brandenburg, K. *Diamond*, Crystal Impact GbR: Bonn, Germany, 2006.
(66) Kim, D.-S.; Han, B., Effect of Junction Temperature on Heat Dissipation of High Power Light Emitting Diodes. *J. Appl. Phys.* **2016,** *119* (12), 125104.
(67) Bain, G. A.; Berry, J. F., Diamagnetic Corrections and Pascal's Constants. *J. Chem. Educ.* **2008,** *85* (4), 532.
(68) Dekker, C.; Arts, A. F. M.; de Wijn, H. W.; van Duyneveldt, A. J.; Mydosh, J. A., Activated Dynamics in a Two-Dimensional Ising Spin Glass: Rb2cu1-Xcoxf4. *Phys. Rev. B* **1989,** *40* (16), 11243-11251.
(69) Cole, K. S.; Cole, R. H., Dispersion and Absorption in Dielectrics I. Alternating Current Characteristics. *J. Chem. Phys.* **1941,** *9* (4), 341-351.
(70) Stephens, P. J.; Devlin, F. J.; Chabalowski, C. F.; Frisch, M. J., Ab Initio Calculation of Vibrational Absorption and Circular Dichroism Spectra Using Density Functional Force Fields. *J. Phys. Chem.* **1994,** *98* (45), 11623-11627.
(71) Becke, A. D., Density-Functional Thermochemistry. Iii. The Role of Exact Exchange. *J. Chem. Phys.* **1993,** *98* (7), 5648-5652.
(72) Clark, T.; Chandrasekhar, J.; Spitznagel, G. W.; Schleyer, P. V. R., Efficient Diffuse Function-Augmented Basis Sets for Anion Calculations. Iii. The 3-21+G Basis Set for First-Row Elements, Li–F. *J. Comput. Chem.* **1983,** *4* (3), 294-301.
(73) Krishnan, R.; Binkley, J. S.; Seeger, R.; Pople, J. A., Self-Consistent Molecular Orbital Methods. Xx. A Basis Set for Correlated Wave Functions. *J. Chem. Phys.* **1980,** *72* (1), 650-654.
(74) Hehre, W. J.; Lathan, W. A., Self-Consistent Molecular Orbital Methods. Xiv. An Extended Gaussian-Type Basis for Molecular Orbital Studies of Organic Molecules. Inclusion of Second Row Elements. *J. Chem. Phys.* **1972,** *56* (11), 5255-5257.
(75) Dolg, M.; Stoll, H.; Preuss, H., Energy-Adjusted Ab Initio Pseudopotentials for the Rare Earth Elements. *J. Chem. Phys.* **1989,** *90* (3), 1730-1734.
(76) te Velde, G.; Bickelhaupt, F. M.; Baerends, E. J.; Fonseca Guerra, C.; van Gisbergen, S. J. A.; Snijders, J. G.; Ziegler, T., Chemistry with Adf. *J. Comput. Chem.* **2001,** *22* (9), 931-967.

(77) Carneiro Neto, A. N.; Moura Jr, R. T., Overlap Integrals and Excitation Energies Calculations in Trivalent Lanthanides 4f Orbitals in Pairs Ln-L (L = ln, N, O, F, P, S, Cl, Se, Br, and I). *Chem. Phys. Lett.* **2020,** *757*, 137884.
(78) Malta, O. L., Mechanisms of Non-Radiative Energy Transfer Involving Lanthanide Ions Revisited. *J. Non-Cryst. Solids* **2008,** *354* (42), 4770-4776.
(79) Longo, R.; Gonçalves e Silva, F. R.; Malta, O. L., A Theoretical Study of the Energy-Transfer Process in [Eu⊂Bpy.Bpy.Bpy]3+ Cryptates: A Ligand-to-Metal Charge-Transfer State? *Chem. Phys. Lett.* **2000,** *328* (1), 67-74.
(80) Malta, O. L.; Gonçalves e Silva, F. R., A Theoretical Approach to Intramolecular Energy Transfer and Emission Quantum Yields in Coordination Compounds of Rare Earth Ions. *Spectrochim. Acta A Mol. Biomol. Spectrosc.* **1998,** *54* (11), 1593-1599.
(81) Malta, O. L., Ligand-Rare-Earth Ion Energy Transfer in Coordination Compounds. A Theoretical Approach. *J. Lumin.* **1997,** *71* (3), 229-236.
(82) Malta, O. L., A Simple Overlap Model in Lanthanide Crystal-Field Theory. *Chem. Phys. Lett.* **1982,** *87* (1), 27-29.
(83) Malta, O. L., Theoretical Crystal-Field Parameters for the Yocl:Eu3+ System. A Simple Overlap Model. *Chem. Phys. Lett.* **1982,** *88* (3), 353-356.
(84) Silva, F. R. G. e.; Malta, O. L., Calculation of the Ligand–Lanthanide Ion Energy Transfer Rate in Coordination Compounds: Contributions of Exchange Interactions. *J. Alloys Compd.* **1997,** *250* (1), 427-430.
(85) Malta, O. L.; Brito, H. F.; Menezes, J. F. S.; Silva, F. R. G. e.; Alves, S.; Farias, F. S.; de Andrade, A. V. M., Spectroscopic Properties of a New Light-Converting Device Eu(Thenoyltrifluoroacetonate)3 2(Dibenzyl Sulfoxide). A Theoretical Analysis Based on Structural Data Obtained from a Sparkle Model. *J. Lumin.* **1997,** *75* (3), 255-268.
(86) de Sá, G. F.; Malta, O. L.; de Mello Donegá, C.; Simas, A. M.; Longo, R. L.; Santa-Cruz, P. A.; da Silva, E. F., Spectroscopic Properties and Design of Highly Luminescent Lanthanide Coordination Complexes. *Coord. Chem. Rev.* **2000,** *196* (1), 165-195.
(87) Macrae, C. F.; Edgington, P. R.; McCabe, P.; Pidcock, E.; Shields, G. P.; Taylor, R.; Towler, M.; van de Streek, J., Mercury: Visualization and Analysis of Crystal Structures. *J. Appl. Crystallogr.* **2006,** *39* (3), 453-457.
(88) Flack, H. D.; Bernardinelli, G., The Use of X-Ray Crystallography to Determine Absolute Configuration. *Chirality* **2008,** *20* (5), 681-690.
(89) Flack, H. D., Chiral and Achiral Crystal Structures. *Helv. Chim. Acta* **2003,** *86* (4), 905-921.
(90) Gregorio, T.; Rudiger, A. L.; Nunes, G. G.; Soares, J. F.; Hughes, D. L., Crystal Structure of an Eight-Coordinate Terbium(Iii) Ion Chelated by N,N'-Bis(2-Hydroxybenzyl)-N,N'-Bis(Pyridin-2-Ylmethyl)Ethylenediamine (Bbpen2-) and Nitrate. *Acta Crystallogr. Sect. E* **2015,** *71* (1), 65-68.
(91) Ayers, K. M.; Schley, N. D.; Ung, G., Solid State Structures, Solution Behavior, and Luminescence of Simple Tetrakis(2-Pyridylmethyl)Ethylenediamine Lanthanide Complexes. *Eur. J. Inorg. Chem.* **2019,** *2019* (33), 3769-3775.
(92) Standley, K. J.; Vaughan, R. A., *Electron Spin Relaxation Phenomena in Solids*. Plenum Press: New York, 1969.
(93) Al Hareri, M.; Ras Ali, Z.; Regier, J.; Gavey, E. L.; Carlos, L. D.; Ferreira, R. A. S.; Pilkington, M., Dual-Property Supramolecular H-Bonded 15-Crown-5 Ln(Iii) Chains: Joint Magneto-Luminescence and Ab Initio Studies. *Inorg. Chem.* **2017,** *56* (13), 7344-7353.
(94) Ren, M.; Xu, Z.-L.; Bao, S.-S.; Wang, T.-T.; Zheng, Z.-H.; Ferreira, R. A. S.; Zheng, L.-M.; Carlos, L. D., Lanthanide Salen-Type Complexes Exhibiting Single Ion Magnet and Photoluminescent Properties. *Dalton Trans.* **2016,** *45* (7), 2974-2982.
(95) Boulon, M.-E.; Cucinotta, G.; Luzon, J.; Degl'Innocenti, C.; Perfetti, M.; Bernot, K.; Calvez, G.; Caneschi, A.; Sessoli, R., Magnetic Anisotropy and Spin-Parity Effect Along the Series of Lanthanide Complexes with Dota. *Angew. Chem. Int. Ed.* **2013,** *52* (1), 350-354.

(96) Abragam, A.; Bleaney, B., *Electron Paramagnetic Resonance of Transition Ions*. Oxford University Press: Oxford, 2012; p 944.
(97) Chen, Y.-C.; Peng, Y.-Y.; Liu, J.-L.; Tong, M.-L., Field-Induced Slow Magnetic Relaxation in a Mononuclear Gd(Iii) Complex. *Inorg. Chem. Commun.* **2019,** *107*, 107449.
(98) Gatteschi, D.; Sessoli, R.; Villain, J., *Molecular Nanomagnets*. Oxford University Press: Oxford, 2006.
(99) Elbjeirami, O.; Rawashdeh-Omary, M. A.; Omary, M. A., Phosphorescence Sensitization Via Heavy-Atom Effects in D10 Complexes. *Res. Chem. Intermed.* **2011,** *37* (7), 691.
(100) Heffern, M. C.; Matosziuk, L. M.; Meade, T. J., Lanthanide Probes for Bioresponsive Imaging. *Chem. Rev.* **2014,** *114* (8), 4496-4539.
(101) Le Fur, M.; Molnár, E.; Beyler, M.; Fougère, O.; Esteban-Gómez, D.; Rousseaux, O.; Tripier, R.; Tircsó, G.; Platas-Iglesias, C., Expanding the Family of Pyclen-Based Ligands Bearing Pendant Picolinate Arms for Lanthanide Complexation. *Inorg. Chem.* **2018,** *57* (12), 6932-6945.
(102) Yanagisawa, K.; Nakanishi, T.; Kitagawa, Y.; Seki, T.; Akama, T.; Kobayashi, M.; Taketsugu, T.; Ito, H.; Fushimi, K.; Hasegawa, Y., Seven-Coordinate Luminophores: Brilliant Luminescence of Lanthanide Complexes with C3v Geometrical Structures. *Eur. J. Inorg. Chem.* **2015,** *2015* (28), 4769-4774.
(103) Xu, J.; Corneillie, T. M.; Moore, E. G.; Law, G.-L.; Butlin, N. G.; Raymond, K. N., Octadentate Cages of Tb(Iii) 2-Hydroxyisophthalamides: A New Standard for Luminescent Lanthanide Labels. *J. Am. Chem. Soc.* **2011,** *133* (49), 19900-19910.
(104) Starck, M.; Kadjane, P.; Bois, E.; Darbouret, B.; Incamps, A.; Ziessel, R.; Charbonnière, L. J., Towards Libraries of Luminescent Lanthanide Complexes and Labels from Generic Synthons. *Chem. Eur. J.* **2011,** *17* (33), 9164-9179.
(105) Brunet, E.; Juanes, O.; Sedano, R.; Rodríguez-Ubis, J.-C., Lanthanide Complexes of Polycarboxylate-Bearing Dipyrazolylpyridine Ligands with near-Unity Luminescence Quantum Yields: The Effect of Pyridine Substitution. *Photochem. Photobiol. Sci.* **2002,** *1* (8), 613-618.
(106) Pham, Y. H.; Trush, V. A.; Carneiro Neto, A. N.; Korabik, M.; Sokolnicki, J.; Weselski, M.; Malta, O. L.; Amirkhanov, V. M.; Gawryszewska, P., Lanthanide Complexes with N-Phosphorylated Carboxamide as Uv Converters with Excellent Emission Quantum Yield and Single-Ion Magnet Behavior. *J. Mater. Chem. C* **2020,** *8* (29), 9993-10009.
(107) Carneiro Neto, A. N.; Teotonio, E. E. S.; de Sá, G. F.; Brito, H. F.; Legendziewicz, J.; Carlos, L. D.; Felinto, M. C. F. C.; Gawryszewska, P.; Moura, R. T.; Longo, R. L.; Faustino, W. M.; Malta, O. L., Chapter 310 - Modeling Intramolecular Energy Transfer in Lanthanide Chelates: A Critical Review and Recent Advances. In *Handbook on the Physics and Chemistry of Rare Earths*, Bünzli, J.-C. G.; Pecharsky, V. K., Eds. Elsevier: 2019; Vol. 56, pp 55-162.
(108) Kovacs, D.; Borbas, K. E., The Role of Photoinduced Electron Transfer in the Quenching of Sensitized Europium Emission. *Coord. Chem. Rev.* **2018,** *364*, 1-9.
(109) Miranda, Y. C.; Pereira, L. L. A. L.; Barbosa, J. H. P.; Brito, H. F.; Felinto, M. C. F. C.; Malta, O. L.; Faustino, W. M.; Teotonio, E. E. S., The Role of the Ligand-to-Metal Charge-Transfer State in the Dipivaloylmethanate-Lanthanide Intramolecular Energy Transfer Process. *Eur. J. Inorg. Chem.* **2015,** *2015* (18), 3019-3027.
(110) Kovacs, D.; Mathieu, E.; Kiraev, S. R.; Wells, J. A. L.; Demeyere, E.; Sipos, A.; Borbas, K. E., Coordination Environment-Controlled Photoinduced Electron Transfer Quenching in Luminescent Europium Complexes. *J. Am. Chem. Soc.* **2020,** *142* (30), 13190-13200.
(111) Wilkinson, A. J.; Maffeo, D.; Beeby, A.; Foster, C. E.; Williams, J. A. G., Sensitization of Europium(Iii) Luminescence by Benzophenone-Containing Ligands: Regioisomers, Rearrangements and Chelate Ring Size, and Their Influence on Quantum Yields. *Inorg. Chem.* **2007,** *46* (22), 9438-9449.
(112) Ferreira, R. A. S.; Nolasco, M.; Roma, A. C.; Longo, R. L.; Malta, O. L.; Carlos, L. D., Dependence of the Lifetime Upon the Excitation Energy and Intramolecular Energy Transfer Rates: The 5d0 Euiii Emission Case. *Chem. Eur. J.* **2012,** *18* (38), 12130-12139.

(113) Kostova, M. H.; Sá Ferreira, R. A.; Ananias, D.; Carlos, L. D.; Rocha, J., Photoluminescent Layered Y(Iii) and Tb(Iii) Silicates Doped with Ce(Iii). *J. Phys. Chem. B* **2006,** *110* (31), 15312-15316.
(114) Beltrán-Leiva, M. J.; Solis-Céspedes, E.; Páez-Hernández, D., The Role of the Excited State Dynamic of the Antenna Ligand in the Lanthanide Sensitization Mechanism. *Dalton Trans.* **2020,** *49* (22), 7444-7450.
(115) El-Sayed, M. A., Spin-Orbit Coupling and the Radiationless Processes in Nitrogen Heterocyclics. *J. Chem. Phys.* **1963,** *38* (12), 2834-2838.
(116) Kasha, M., Characterization of Electronic Transitions in Complex Molecules. *Discuss. Faraday Soc.* **1950,** *9* (0), 14-19.
(117) Zhang, D.; Zhao, Q.; Zang, J.; Lu, Y.-J.; Dong, L.; Shan, C.-X., Luminescent Hybrid Materials Based on Nanodiamonds. *Carbon* **2018,** *127*, 170-176.
(118) Wang, T.; Li, H., A Simple and Green Strategy for Preparing Luminescent Tb3+ Complex-Based Nanocomposite with Stable Luminescence in Water. *Mater. Res. Bull.* **2017,** *93*, 28-34.
(119) Xu, Q.; Li, Z.; Li, H., Water-Soluble Luminescent Hybrid Composites Consisting of Oligosilsesquioxanes and Lanthanide Complexes and Their Sensing Ability for Cu2+. *Chem. Eur. J.* **2016,** *22* (9), 3037-3043.
(120) Lima, P. P.; Nolasco, M. M.; Paz, F. A. A.; Ferreira, R. A. S.; Longo, R. L.; Malta, O. L.; Carlos, L. D., Photo–Click Chemistry to Design Highly Efficient Lanthanide B-Diketonate Complexes Stable under Uv Irradiation. *Chem. Mater.* **2013,** *25* (4), 586-598.
(121) Kai, J.; Felinto, M. C. F. C.; Nunes, L. A. O.; Malta, O. L.; Brito, H. F., Intermolecular Energy Transfer and Photostability of Luminescence-Tuneable Multicolour Pmma Films Doped with Lanthanide–B-Diketonate Complexes. *J. Mater. Chem.* **2011,** *21* (11), 3796-3802.
(122) Lapaev, D. V.; Nikiforov, V. G.; Lobkov, V. S.; Knyazev, A. A.; Galyametdinov, Y. G., A Photostable Vitrified Film Based on a Terbium(Iii) B-Diketonate Complex as a Sensing Element for Reusable Luminescent Thermometers. *J. Mater. Chem. C* **2018,** *6* (35), 9475-9481.
(123) Nolasco, M. M.; Vaz, P. M.; Freitas, V. T.; Lima, P. P.; André, P. S.; Ferreira, R. A. S.; Vaz, P. D.; Ribeiro-Claro, P.; Carlos, L. D., Engineering Highly Efficient Eu(Iii)-Based Tri-Ureasil Hybrids toward Luminescent Solar Concentrators. *J. Mater. Chem. A* **2013,** *1* (25), 7339-7350.
(124) Fang, M.; Bispo-Jr, A. G.; Fu, L.; Ferreira, R. A. S.; Carlos, L. D., Efficient Green-Emitting Tb3+-Doped Di-Ureasil Coating Phosphors for near-Uv Excited Light-Emitting Diodes. *J. Lumin.* **2020,** *219*, 116910.
(125) Nolasco, M. M.; Vaz, P. M.; Vaz, P. D.; Ferreira, R. A. S.; Lima, P. P.; Carlos, L. D., A Green-Emitting A-Substituted B-Diketonate Tb3+ Phosphor for Ultraviolet Led-Based Solid-State Lighting. *J. Coord. Chem.* **2014,** *67* (23-24), 4076-4089.
(126) Chen, Y.; Wai Cheah, K.; Gong, M., Low Temperature Quenching and High Efficiency Tm3+, La3+ or Tb3+ Co-Doped Casc2o4:Ce3+ Phosphors for Light-Emitting Diodes. *J. Lumin.* **2011,** *131* (8), 1770-1775.
(127) Sun, N.; Li, L.; Yang, Y.; Zhang, A.; Jia, H.; Liu, X.; Xu, B., Synthesis, Characteristics and Luminescent Properties of a New Tb(Iii) Ternary Complex Applied in near Uv-Based Led. *Opt. Mater.* **2015,** *49*, 39-45.
(128) Sun, N.; Zhao, X.; Yang, Y.; Li, L.; Zhang, A.; Jia, H.; Liu, X., Synthesis and Luminescent Properties of Terbium Complex Containing 4-Benzoylbenzoic Acid for Application in Nuv-Based Led. *J. Rare Earths* **2016,** *34* (2), 130-136.
(129) Jang, H. S.; Won, Y. H.; Jeon, D. Y., Improvement of Electroluminescent Property of Blue Led Coated with Highly Luminescent Yellow-Emitting Phosphors. *Appl. Phys. B* **2009,** *95* (4), 715-720.
(130) Jang, H. S.; Im, W. B.; Lee, D. C.; Jeon, D. Y.; Kim, S. S., Enhancement of Red Spectral Emission Intensity of Y3al5o12:Ce3+ Phosphor Via Pr Co-Doping and Tb Substitution for the Application to White Leds. *J. Lumin.* **2007,** *126* (2), 371-377.

For Table of Contents Only

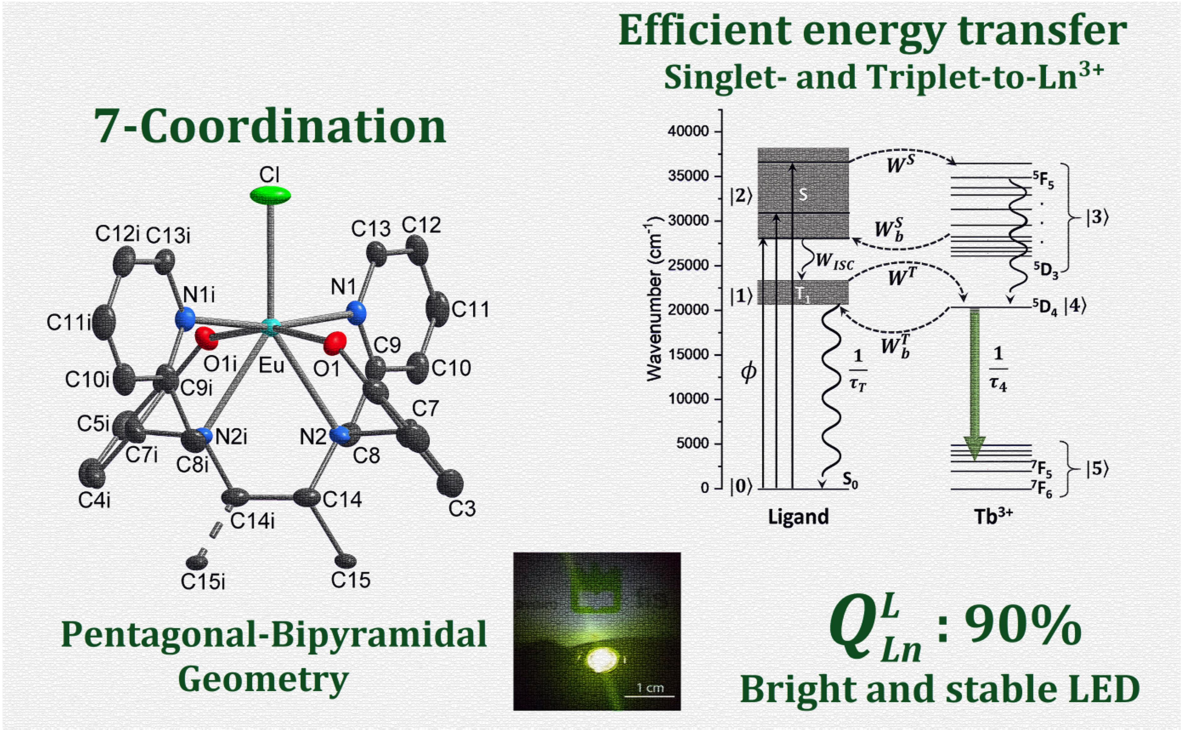

Synopsis

This work presents a comprehensive structural, chemical, and spectroscopic characterization of two Tb^{3+} complexes of mixed-donor, ethylenediamine-based ligands, focusing on their outstanding optical properties. They constitute good molecular examples in which both triplet and singlet excited states provide energy to the Tb^{3+} ion and lead to high values of Q_{Ln}^{L}.